A practical method to characterize Proton Exchange Membrane Fuel Cell catalyst layer topography: application to two coating techniques and two carbon supports

Fabien L. Deschamps ConceptualizationData curationFormal analysisInvestigationMethodologyVisualizationSoftw
Julien G. Mahy Data curationFormal analysisInvestigationVisualizationWriting - original draftWriting - review & editi
Alexandre F. Léonard Data curationMethodologyWriting - original draftWriting - review & editing ,
Stéphanie D. Lambert Data curationProject administrationResourcesWriting - original draft ,
Adrien Dewandre Data curationFormal analysisInvestigationWriting - original draft ,
Benoît Scheid Data curationFormal analysisInvestigationMethodologyWriting - original draft ,
Nathalie Job ConceptualizationData curationFormal analysisFunding acquisitionInvestigationMethodologyProject a

PII: S0040-6090(19)30776-X
DOI: https://doi.org/10.1016/j.tsf.2019.137751
Reference: TSF 137751

To appear in: *Thin Solid Films*

Received date: 25 June 2019
Revised date: 2 December 2019
Accepted date: 11 December 2019

Please cite this article as: Fabien L. Deschamps ConceptualizationData curationFormal analysisInvestigationMetho
Julien G. Mahy Data curationFormal analysisInvestigationVisualizationWriting - original draftWriting - review & editi
Alexandre F. Léonard Data curationMethodologyWriting - original draftWriting - review & editing ,
Stéphanie D. Lambert Data curationProject administrationResourcesWriting - original draft ,
Adrien Dewandre Data curationFormal analysisInvestigationWriting - original draft ,
Benoît Scheid Data curationFormal analysisInvestigationMethodologyWriting - original draft ,
Nathalie Job ConceptualizationData curationFormal analysisFunding acquisitionInvestigationMethodologyProject a
A practical method to characterize Proton Exchange Membrane Fuel Cell catalyst layer topography: application to two coating techniques and two carbon supports, *Thin Solid Films* (2019), doi: https://doi.org/10.1016/j.tsf.2019.137751

HIGHLIGHTS

- Proton Exchange Membrane Fuel Cell coatings prepared by film casting and spraying
- The topography was characterized by profilometry and 3D laser scanning microscopy
- Methods were developed for accurate 3D data processing
- A comparison has been made between these two 3D profile characterization techniques
- The complementarity of these two techniques was demonstrated

A practical method to characterize Proton Exchange Membrane Fuel Cell catalyst layer topography: application to two coating techniques and two carbon supports

Fabien L. Deschamps[a], Julien G. Mahy[a], Alexandre F. Léonard[a], Stéphanie D. Lambert[a], Adrien Dewandre[b], Benoît Scheid[b], Nathalie Job[a,*]

[a] *University of Liège, Department of Chemical Engineering – Nanomaterials, Catalysis, Electrochemistry (NCE), building B6a, Quartier Agora, Allée du six Août 11, 4000 Liège, Belgium*

[b] *Université libre de Bruxelles, Transferts, Interfaces et Procédés (TIPs), Avenue F.D. Roosevelt 50, 1050 Brussels, Belgium*

***Corresponding author:** Nathalie Job, University of Liège, Department of Chemical Engineering – Nanomaterials, Catalysis, Electrochemistry (NCE), building B6a, Quartier Agora, Allée du six Août 11, 4000 Liège, Belgium. E-mail address: Nathalie.Job@uliege.be. Tel: +32 4 366 35 37.

Abstract

The coating technique and the type of carbon support can strongly affect the surface topography, the homogeneity and the thickness of the catalyst layers of Proton Exchange Membrane fuel cells. These features can in turn strongly modify the local diffusion properties of the layer and the final cell performance, but literature about catalytic layers does not often address such issues. This work aims at studying the topography of proton exchange membrane fuel cell catalyst layers by means of 3D characterization methods. For that purpose, two types of slurries, made of Nafion® and carbon black or a carbon xerogel, have been coated on a Kapton® sheet by film-casting and by spray-coating. The surface topography of the samples was characterized by contact profilometry and 3D laser scanning microscopy. The data obtained with both methods were processed in order to obtain accurate 3D representations of the surface of the layers. Contact profilometry allows to perform measurements over the entire surface of the sample (5 cm $\times$ 5 cm). Layers obtained by film-casting turn out to be very smooth, but also thinner at the edges of the coating. For layers prepared by spray-coating, the reproducibility and the homogeneity are improved; however, the surface displays a higher roughness. With 3D laser scanning microscopy measurements, only a small part of the sample was analyzed (0.25 cm^2) with a high definition, allowing to characterize more precisely the surface topography. The comparison of both techniques has been enriched by the simulation of the profilometer tip motion at the surface of the observed 3D microscopy profile, giving insight into the

observed differences. The 3D microscopy measurements proved to be more accurate, but not representative of the whole sample, especially for less homogeneous layers prepared by film-casting.

Keywords: Proton Exchange Membrane Fuel Cell catalyst layer, carbon xerogel, 3D microscopy, profilometry, 3D profile

1. Introduction

The Proton Exchange Membrane Fuel Cell (PEMFC) is a very promising solution for electricity generation in transportation and stationary applications [1–3]. Its principle relies on the oxidation of hydrogen (at the anode) and the reduction of oxygen (at the cathode), while a proton-conducting membrane (Nafion®, usually) allows for the charge transport in-between. In order to increase the kinetics of the Hydrogen Oxidation Reaction and the Oxygen Reduction Reaction, catalyst layers are required at both the electrodes.

A catalyst layer of a PEMFC is a composite material generally made of platinum nanoparticles supported on a porous carbon, Nafion® as a binder and ionic conductor and a void fraction derived from the carbon porosity and the evaporation of the solvent after the coating process [4]. In some cases, polytetrafluoroethylene (PTFE) is also added in order to increase the hydrophobicity and thus allows for a better evacuation of the water produced in the catalyst layer [5]. In most preparation methods, platinum nanoparticles are synthesized or deposited on a porous carbon support [6–9]. Carbon blacks are the most commonly used carbon carriers in fuel cells and, in particular, Vulcan® XC-72 from Cabot remains the reference material in the PEMFC literature [10].

In addition to carbon blacks, other synthetic carbon materials are under study in order to improve performance and to optimize the utilization of platinum [11–13]. The most widely studied are carbon nanotubes, nanospheres or nanofibers, as well as graphene, ordered mesoporous carbons and carbon gels [11–14]. In this work, carbon xerogels will be used as support [6]. These are composed of amorphous carbon nodules with small graphitic domains [15]. These nodules are joined to each other by covalent bonds between carbon atoms so that their assembly forms a porous monolith with good mechanical resistance. While the space between the different aggregates composing a catalyst layer prepared from carbon black strongly depends on the electrode processing, the pore texture properties of layers prepared from carbon gels is set by the carbon material synthesis: the pore texture of the catalyst layer itself is in this case independent of its processing mode [16,17]. They can therefore be considered as good model materials to study the influence of pore sizes in fuel cells.

Since the composition of the catalyst layers strongly influences their final properties in fuel cell operation, a large number of studies relate to the influence of the Nafion® percentage by weight or

Nafion® to carbon ratio (N/C) in the catalyst layer. When these values increase, the ionic conductivity is improved, but the porosity decreases, as well as the accessibility of the gases to the platinum nanoparticles [18]. The optimum values of mass percentage in Nafion® generally accepted are between 30 and 36 wt.% [19,20]. Optimal N/C ratios vary from one study to another, but the values are usually comprised between 0.3 and 1 [7,19,21–23]. The nature and proportions of solvents can also influence on the morphology of the catalyst layer [22]. Whatever the support used (Gas Diffusion Layer, membrane or inert support), the deposition of catalyst layers can be performed by different techniques such as cathodic pulverization [24,25], electrodeposition [26] or wet chemistry methods (spray-, bar-, spin-coating) [27–30]. The spray, which can be manual or robotic [27,29,31], consists in atomizing the ink into fine droplets on the substrate. Coatings can be realized on the entire desired surface, usually in multiple passes, with a good reproducibility. A mask deposited on the substrate allows to define the geometry of the deposit. The bar-coater [28,30] is a method allowing to spread the ink on a substrate fixed on a flat surface. A mask can also be used to define the geometry of the deposit. This technique is regularly used to produce catalyst layers of PEMFC at laboratory scale because of its low cost, easy implementation and high versatility.

The morphology, homogeneity and reproducibility of coatings can vary strongly with the techniques used as well as the associated operating variables. However, the majority of the studies related to that topic focus on the performance in PEMFC conditions without taking into account the morphology of the final catalyst layers produced. It seems nevertheless that an in-depth study of the surface morphology should allow for a better understanding of the link between the deposition technique used, the surface state and the final performance in PEMFC. Among the literature dealing with deposition techniques or the study of morphologies [22,28,30,32–37], Scanning Electron Microscopy is the most widely used. Indeed, it allows to visualize the surface homogeneity, the porosity and the possible presence of cracks, while observations made on cross-sections can give an estimate of the thickness of the coatings. The very local nature of this observation technique does however not allow for any precise quantification of pore texture parameters and could very well not be representative of the whole sample. Cracks or detachment of part of the deposit can also be visualized by light microscopy [30]. Atomic Force Microscopy can also be used to measure the roughness of the surface [38]. X-ray microtomography [38,39] allows to reconstruct the 3D morphology of a catalyst layer; however the resolution as described in the two cited references allows only to visualize cracks and the largest pores (~ 5 µm). Paradoxically, PEMFC catalyst layer characterization by profilometry measurements are much less frequent, probably because this technique requires to produce coatings on very flat model surfaces.

As seen from these examples, there is a lack of in-depth and complete characterizations of the topography of catalyst layers for PEMFCs in the majority of the studies described. In particular, this work will focus on the characterization of the homogeneity of the thickness and the roughness of the 3D profiles of the PEMFC catalytic layers. The aim of this work is to study the 3D surface topography of catalyst layers for PEMFC application with a critical view on the interpretation of the results. To that purpose, it was decided to produce catalyst layers using two popular deposition techniques: film-casting and spray-coating. In addition, both a commercial carbon black and a homemade carbon xerogel were used in order to put in light the influence of the carbon nature, morphology and granulometry on the homogeneity of the coatings and the pertinence of the results from characterizations. Two different techniques were used for 3D surface profile constructions: the profilometry and the 3D laser scanning microscopy. For each technique, the data were corrected to reproduce a more accurate 3D profile of the samples. The method of the 3D profile reconstruction is described and widely explained. A comparison of both measurement techniques is made as well as the comparison of the two deposition methods. The innovation of this work comes mainly from the study of the surface profile that is put in relationship with the deposition technique, which is barely referenced in the literature for PEMFC catalyst layers.

2. Materials and methods

2.1. Xerogel synthesis and grinding

The carbon xerogel material is synthesized following the procedure described by Job *et al*. [40]. 114.7 g of Resorcinol (Merck for synthesis) are added to 214.5 g of ultra-pure water (18 MΩ.cm). Then, 0.074 g of Na_2CO_3 (Acros Organics, 99.5% extrapure, anhydrous) is added to set the pH, which determines the pore size of the final carbon xerogel [42]. The solution is then mixed with 169.1 g of an aqueous formaldehyde solution (Sigma Aldrich, ACS reagent 37 wt.% in water, contains 10–15% methanol as stabilizer), the molar ratio between resorcinol and formaldehyde is 0.5. The mixture is stirred for 1h. The dilution ratio D (Water/reactants) is fixed at 5.7.

The solution is aged in sealed vials for 72 h at 85°C for gelation. Then, the gel is dried under vacuum at 60°C for 12 h and 150°C for 30 h. An organic monolith polymer is obtained.

A part of the dried xerogel is then ground using a Fritsch planetary mill (Mono Mill P6) in agate jars with 1 cm diameter balls following the procedure described in a previous work to obtain homogenous and reproducible particle sizes [43]. Afterwards the grinded powder is pyrolyzed under nitrogen at 800°C following [41], this way is called the *dry way* of grinding.

The second part of dried powder is directly pyrolyzed under nitrogen at 800°C following the program detailed in reference [41]; the obtained carbon is then grinded with isopropanol using a Retsch PM 400 planetary mill in zirconium oxide jars with 1 mm diameter balls, leading to the *liquid way* of grinding.

The particle size distributions of the powders are obtained using laser diffraction with a Mastersizer 2000 (Malvern Instruments) in wet mode (Hydro2000). Prior to grain size distribution measurements, the samples are dispersed in water using high intensity ultrasonic irradiations (Hielsher, UP400S). The sample preparation method is described elsewhere [41] . Particle size distribution was obtained from the raw data by mathematic treatment assuming a spherical geometry of the particles [41].

The particle size distributions for the two ways of grinding are represented in Figure 1. Two particle sizes are obtained: 7 µm and 0.5 µm for the dry and liquid ways respectively. The distributions are a little bit spread so bigger particles are also present. In the liquid grinding, a smaller particle population is also observed.

2.2. Ink composition

The inks for the layer deposition are composed of carbon powder, Nafion® (Liquion® LQ-1115 1100 EW 15 wt.% in water/isopropanol or DE2021 20 wt.% in water/isopropanol, both from DuPont®), ultrapure water (MilliQ, 18MΩ) and isopropanol (ACROS, 99.5%, extra dry). In this work, the weight ratio between Nafion® and carbon was set to 1. Pt was not added because its influence on the catalyst layer morphology is negligible. All inks were kept under stirring during 1 h before being processed.

The composition of the various inks and the coating procedure are depicted in Table 1. The amount of carbon in the ink was higher for film-casting than for spray-coating, since the viscosity needs to be higher in the former case. Only one pass was made for the film-casting, while 160 or 320 were made in the case of spray-coating. Both the commercial carbon (XC-72R from Cabot®) and the homemade carbon xerogel (X85, with a mean particle size, obtained after grinding, equal to either 0.5 or 7 µm) were used. The latter material was synthesized following the method described by Job *et al.* [40] leading to a carbon xerogel with an average pore size of 85 nm and a macropore volume of 1.8 $cm^3 g^{-1}$. In order to produce two samples with two different mean particle sizes, the carbon xerogel underwent two different grinding procedures [41]. The mean particle sizes were 0.5 and 7 µm respectively for both samples (Figure 1).

The used carbon samples are denoted as follows. The first letter corresponds to the technique used for deposition (F for film-casting and S for spray-coating); this letter is followed by the acronym of the carbon used (XC72R or X85). For the homemade carbon xerogels, the name is followed by the average particle size obtained after grinding (0.5 or 7 µm). For sample S_X85_0.5µm, 2 layers of different thickness were prepared, leading to samples named S_X85_0.5µm_A (160 spray passes) and S_X85_0.5µm_B (320 spray passes). A total of 6 coatings are obtained, as denoted in Table 1.

2.3. Coating procedures

Two coating procedures were used to assess their influence on the resulting surface topography of the PEMFC catalyst layers: film-casting and spray-coating. In each case, a Kapton® sheet was used as a support.

2.3.1. Film-casting

A simplified version of the bar-coating method was used in the present work, it will be called film casting. Indeed, a film applicator was used instead of a bar for coatings. An Elcometer 4340 bar-coating device together with an Elcometer 3580 film applicator was used for that purpose. The setup is composed of a perfectly flat perforated vacuum table that allows for keeping the support in place; a motorized tray is used to push the casting knife film applicator at selectable and constant speed. A picture and a scheme of the experimental setup are shown in Figure 2.

In order to limit the mechanical constraints on the support and to homogenize the depression imposed by the table, a 70 µm thick porous fabric made of glass fibers impregnated with PTFE was placed on the suction surface; then the 7 cm × 7 cm Kapton® support was placed on top of it. In order to prepare a 5 cm × 5 cm coating, a non-porous 140 µm PTFE-impregnated glass fiber mask with a window of 5 cm × 5 cm was centered on the Kapton® sheet (see Figure 3). All of these elements are kept perfectly flat thanks to the vacuum table. The ink was deposited on the mask, then spread by the casting knife placed on the mask of 140 µm of thickness. The total height of the ink deposited on the Kapton® was 200 µm by adjusting the knife height. Deposits were made at room temperature (about 20 °C).

2.3.2. Spray-coating

The principle of this technique is to spray an ink on the Kapton® support with a nozzle mounted on a robotic arm. A Nordson EFD 781 nozzle with a 781S-SS tip was used. The flow rate of the ink was controlled by a syringe pump to impose a constant flow of 12 µL s^{-1}. The air flow for spraying the ink was controlled by a pressure regulator set at 41 kPa.

The 7 cm × 7 cm Kapton® substrate was mounted on an aluminum plate of adjustable temperature, with a measured value of 91 °C. This high temperature is necessary to evaporate the solvent between each pass. A mask, made of non-porous glass fiber impregnated with PTFE, defining a 5 cm × 5 cm window was centered and placed on the Kapton® support. Metal blocks were arranged on each side of the 5 cm × 5 cm window to keep the assembly in place during the spraying process.

The course imposed on each pass by the robotic spray consisted of 18 parallel lines of a length of 7 cm and a width of 2 mm between each step to form a 7 cm × 7 cm square (Figure 4b) at a speed equal to 15.1 cm s^{-1}. The nozzle was positioned at 33 mm in height. At this height, the deposit area covered by the nozzle is approximately 1 cm^2, and has a circular shape. A margin of 1 cm is necessary on each edge of the 5 cm × 5 cm coating to obtain a constant thickness over the whole sample surface, especially on the edges of the electrode. After each full pass on the sample, the spray moves away to a distance of 9 cm from the deposit (8 cm + the 1 cm margin) before going back to the initial position; this step is meant to prevent altering the edges of the layer at each pass (see Figure 4b). Indeed, the airflow itself tends to erode the layer over time. Experiments described in Figures 4 and 5 highlight this erosion phenomenon.

Indeed, Figure 5 compares the profilometry results as described in section 3.1 for the composition S_XC72R with the two different courses (presented in Figures 4a and 4b). The layer thickness in Figure 5a is not homogeneous one both sides: one is thinner than the other due to the return of the spray to its initial position (left edge of Figure 4a). This shows that the spray partly erodes the deposit during successive passages next to the layer. This phenomenon is not present (Figure 5b) for coatings realized following the trace of Figure 4b, far away from the layer edge. Overall, these results show that the method of thickness measurement on the whole sample described in section 3.1 is very effective to check and improve the homogeneity of a coating process.

The number of passes and the ink concentration, presented in Table 1, allow to determine the layer thickness.

2.4. Characterization techniques

2.3.1 Profilometry

The homogeneity of the coatings was assessed by stylus profilometry. However, a direct measurement of the catalyst layer does not allow determining the thickness of the sample. Indeed, being non-rigid, Kapton® bends, even on a perfectly flat surface. The preparation of the sample (Figure 6) consists thus in removing parallel strips of catalyst layer with a toothpick. These strips were approximately 250 µm wide over the entire length of the sample, and spaced 1 or 2 mm apart (Figure

6b). The landmarks formed by these bare strips allowed to determine the baseline of the support and to deduce the thickness of the deposit over the entire width of the sample. Perpendicular to these strips, ten measurements were performed at intervals of 5 mm and over a distance of 54 mm (Figure 6c) using a Veeco Dektak 8 contact profilometer. The principle of this technique is based on the displacement and measurement of the height of a tip forming a hemisphere and in contact with the sample. The stylus (12.5 µm radius) applies a force of 1 mg (9.81 µN) and moves at a speed of 300 µm s^{-1}; its vertical position is recorded every 1 µm in the X-Y plane. The integrity of the coating after profilometry characterization has been assessed by three successive measurements on same line on one sample; those successive measurement showed that the tip passage does not change the sample profile, ruling out any bias due to the surface modification during measurement.

2.3.2 3D laser scanning microscopy

For the confocal 3D laser scanning microscopy measurement, a Keyence VK-X200 device was used. This method consists in focusing a laser at a defined height and measuring the intensity of the reflected light. The focused spot light scans the image area within the field of view divided into a number of pixels (X-Y plane parallel to the sample), the reflected light at each pixel being detected by a photoreceptor. This operation is repeated a large number of times upon shifting the focusing height of the laser by 0.5 nm according to the Z axis (*i.e.* perpendicular to the sample surface). For each pixel, the highest intensity is obtained when the focusing height of the laser corresponds to the height of the sample at this given pixel. The height at each pixel can thus be determined with a resolution of 0.5 nm by determining the maximum intensity reflected as a function of Z. The wavelength of the laser is 408 nm. The purpose of these measurements is to use a non-contact thickness characterization method to assess the accuracy and relevance of contact profilometry measurements.

Given the time required for image processing, only a selection of representative samples were characterized by this technique. Samples F_X85_0.5µm, F_XC72R and S_XC72R were observed with a 50 × magnification lens. Sample S_X85_7µm was characterized with a 150 × magnification lens. In all cases, the measured surface was approximately 0.25 cm² and was located at the center of the 5 cm × 5 cm coating. These samples were prepared for profilometry and thus displayed strips where the deposit was removed every 1 or 2 mm (Figure 6c). The measuring surface was selected so as to include two strips in order to correct the obtained signal for the non-flatness of the support.

3 Results and discussion

3.1 Profilometry measurement processing

In order to obtain a 3D surface topography, profilometry measurements need to be processed to reconstruct the 3D signals from the 2D measurements. Furthermore, the profilometry measurements need some corrections to be as close as possible to the actual profile. Indeed, different correction algorithms [44,45] can be used for surface reconstruction; those algorithms may be rather complex, depending the tip geometry. In the present work, an algorithm similar to that of Lee *et al.* [46] was applied in order to reconstruct the 3D profile obtained using a spherical tip.

Indeed, the contact profilometry method consists in moving a diamond tip forming a half-sphere (12.5 µm in radius) at the sample surface. The variation of the height of the tip between the areas with and without deposit allows to deduce the thickness of the coating (Figure 7a). However, the tip does not always touch the sample at the lowest part of the hemisphere (Figure 7b), which leads to an overestimation of the height of the sample at this position.

Figures 8b, 8c and 8d show how the width of a peak can be overestimated by the tip of the profilometer and that some areas, for which the thickness is inevitably overestimated, can be detected (Figure 8e). Finally, the signal can be partially corrected taking into account the shape of the tip in order to get closer to the actual topography of the coating (Figure 8f).

Concretely, each measurement (*e.g.* A in Figure 8e) defines a mandatorily empty area occupied by the tip. Therefore, any measured point located above the shape of the tip (*e.g.* B in Figure 8e) is necessarily an overestimated measurement of the sample height. This overestimated value of the coating thickness can be partially corrected by assigning a height equal to that of C to the same position of the sample. An algorithm was therefore developed to correct all the measurements that are detected as overestimated. The profile obtained by profilometry being in 2 dimensions, the tip is modelled by a half-disk (12.5 µm in radius). *Via* the algorithm, the height of each measured point corresponding to a position located above the blue half-circle (Fig. 3e) is modified as the height corresponding to the highest possible position, *i.e.* the height corresponding to C. The details of the calculation to build the algorithms are explained in the following paragraphs.

Figure 9 schematizes a portion of a measured profile $p(x)$ (in black). The semicircle $c(x)$ (in blue) corresponds to the shape of the profilometer tip in contact with A. B corresponds to the center of the semicircle of radius r. Calculation is detailed for any position of A; however, this has to be carried out for each point of the profile $p(x)$. Since the coordinates of A are known, those of B are determined from the position of A and the disk radius r (Equations 1 and 2).

$$x_B = x_A \quad (1)$$

$$y_B = y_A + r \quad (2)$$

The equation of the half-circle c(x) of center B is calculated using that of a circle, *i.e.*:

$$(x - x_B)^2 + (c(x) - y_B)^2 = r^2 \quad (3)$$

which leads to two possible height values for each value of *x*:

$$c(x) = y_B \pm \sqrt{r^2 - (x - x_B)^2} \quad (4)$$

Considering the lower semicircle, one deduces:

$$c(x) = y_B - \sqrt{r^2 - (x - x_B)^2} \quad (5)$$

Then, the corrected profile *p*'(*x*) is determined as:

$$\forall\, x_B - r < x < x_B + r : p'(x) = \min[c(x); p(x)] \quad (6)$$

In other words, *p*'(*x*) is initialized as *p*(*x*); then the algorithm checks, for each *c*(*x*) curve, whether new lower values are found. If new lower values are detected, these replace the previous ones in *p*'(*x*).

An example (sample S_X85_7µm) is also presented in Figure 10 which compares a profile portion of a layer deposited on Kapton® (S_X85_0.5µm_A sample), before and after correction of the shape of the tip. The difference between the two profiles is essentially visible on the highest peaks.

The impact of this data processing is more pronounced on the roughness than on the average thickness of the samples. Indeed, the differences between the corrected and uncorrected signals range from 0.1 to 4.1 % for the average thickness and from 2.4 to 24.8 % for the roughness, depending on the sample analyzed.

Figure 11a shows an example of a complete thickness profile, measured on S_XC72R sample (250 µm removed every 1 mm) after correction of the tip shape. Areas where the coating was removed show that the support is not perfectly flat. However, the roughness of these naked areas is very low, which seems to indicate that Kapton® is not damaged while removing the coating with the toothpick. A precise measurement of the sample thickness over its length can finally be obtained by subtracting the shape of the Kapton® support, as a second step of the signal processing as described below.

Figure 11b shows the data obtained from the profilometer and corrected from the tip shape. To correct for the profile of the support, in a first instance, a point is selected at the beginning and at the end of each zone where the layer was removed (Figure 11c). Then, between two selected points A and B (corresponding to two red squares on Figure 11c, A and B for example), a baseline is subtracted in order to set the ordinate of A and B at 0. Equation 7 is thus applied to any point between A and B:

$$Z_{corrected} = Z_{uncorrected} - Z_A \frac{X_B - X}{X_B - X_A} - Z_B \frac{X - X_A}{X_B - X_A} \quad (7)$$

where X_A, X_B, Z_A and Z_B are the coordinates (abscissa and ordinate, respectively) of the two reference points of the base line, X and $Z_{uncorrected}$ represent the coordinates of a point between A and B, and $Z_{corrected}$ corresponds to the ordinate of the same point after correction.

This method was used on each point of the profile to fully flatten the curve (Figure 11b to d). The spacing between naked zones was initially set at 1 mm (first 4 samples). Afterwards, this variable was increased to 2 mm, which is sufficient to obtain a good approximation of the shape of the support while saving time during sample preparation and data analysis. Finally, the edges of the coated areas sometimes display peaks corresponding to a material re-deposition during the sample preparation: indeed, removed material may stick to the coating and is then detected by the profilometer (Figure 11e). For each discrete zone containing *n* points (between two green disks), the average values of thickness and roughness were calculated. The roughness, R_q , corresponds to the root mean square of the height:

$$R_q = \sqrt{\frac{1}{n}\sum_{k=0}^{n}(Z_k - Z_m)^2} \quad (8)$$

where n is the number of points in the zone with coating, Z_k is the height of point k and Z_m is the mean height of the *n* points.

This treatment was performed on ten parallel profiles along each sample using a Microsoft Excel® macro to partially automate these steps. The ten profiles being identically spaced (5 mm) and starting on the same side of the layer, coordinates (X, Y) were assigned to each average value of the thicknesses of the ten profiles and grouped in a three-column matrix (X, Y, Z). These values were then interpolated to obtain a surface, as shown in Figure 12 for all the studied samples. However, this surface is an interpolation of the average values of the thickness measured over approximately 1

mm. The actual surface is rougher, but the average calculated values are sufficient to check for the thickness and the homogeneity of the samples.

3.2 Comparison of the results from profilometry measurements on samples prepared by film-casting and spray coating

Figure 12 shows the calculated surfaces of coatings obtained from the two carbon materials and using either film-casting or spray-coating. At a first glance, it can be seen that spray-coating (Figures 12b, 12d, 12e and 12f) allows to obtain deposits with a constant average thickness over the entire surface. In contrast, the coatings resulting from film-casting (Figure 12a and 12c) are much less homogeneous. Indeed the thickness is systematically lower at the edges. This phenomenon is even underestimated on the figures because the 3D profiles presented correspond to a surface of 4.75 cm $\times$ 4.75 cm and not 5 cm $\times$ 5 cm due to the positioning of the ten measurements (separated by 0.5 cm each) on the samples. In addition, the deposits are generally thicker where drying takes more time, which is usually the case in the middle of the sample (Figure 12a). The non-planarity of the support during deposition or a non-controlled ambient air flow can also account for preferential drying of some areas. In addition, carbon particles or Nafion® could be transferred to wet areas by capillarity.

The supports were weighed before and after deposition using an air ionizer to eliminate the electrostatic charges present on the Kapton® support. The masses obtained are grouped in Table 1, whereas the average values of thickness and roughness are presented in Table 2. For samples F_XC72R, S_XC72R, F_X85_0.5µm and S_X85_0.5µm_A, the variables of the deposition process are identical for a same deposition technique. The type of carbon has no significant influence on the masses deposited for each technique, but the average thickness is in each case higher for the spray-coating. This is probably due to differences in the drying mechanisms between film-casting (where all the solvent is present at the beginning) and the spray-coating (where the solvent is progressively eliminated between passes). Coatings made of carbon xerogels are also less dense than carbon black deposits: this is due to the large pore volume of the former.

Figure 13 compares portions of the 2D profiles for the four first samples of Table 2 (F_XC72R, S_XC72R, F_X85_0.5µm and S_X85_0.5µm_A), which display similar masses of coatings. These 2D profiles clearly illustrate the differences in roughness between samples prepared by film-casting and spray-coating. The spray-coating method leads to deposits with a higher void fraction, which explains the higher roughness and the lower density. Such a difference in texture can significantly influence the mass transport within the catalyst layer. This again shows the necessity to take into account a full

characterization of the surface morphology when conclusions are drawn regarding the activity of a PEMFC catalyst layer.

The comparison of S_X85_0.5µm_A and S_X85_0.5µm_B samples illustrates the influence of the number of spray passes for deposits prepared from the carbon xerogel (Table 2), the composition of the ink being the same for both samples. This example shows that the spray is a very flexible technique for choosing the thickness (or the mass) of a coating. Between the two experiments, both the mass and the thickness are doubled when the number of passes is doubled (Table 1), showing that the density remains constant over deposition time (Table 2). Figures 12d and 12e show the comparison of the 3D profiles of these two deposits: both display a good homogeneity in thickness.

3.3 Processing of the 3D laser scanning microscopy data

As for the profilometry measurements, the shape of the support needs to be corrected from the 3D laser scanning microscopy profiles. To illustrate this statement, Figure 14 shows the 3D profile of F_XC72R sample before correction. Areas without coating (in blue) allow to deduce the shape of the support. The mean height of the support is calculated at the four corners of the measured area as depicted on Figure 14 (labels a, b, c, and d). The surface is then corrected as follows.

In a first step, the raw data are corrected by applying Equation 9 to all points of the graph:

$$Z'_k = Z_k - d\frac{X_k}{X_{tot}}\frac{Y_k}{Y_{tot}} - c\frac{(X_{tot}-X_k)}{X_{tot}}\frac{Y_k}{Y_{tot}} - b\frac{X_k}{X_{tot}}\frac{(Y_{tot}-Y_k)}{Y_{tot}} - a\frac{(X_{tot}-X_k)}{X_{tot}}\frac{(Y_{tot}-Y_k)}{Y_{tot}} \quad (9)$$

where X_k, Y_k, and Z_k are the coordinates of a point k of the graph. Z'_k is the calculated corrected height. a, b, c, and d are the heights of the support at the four corners of the 3D profile. X_{tot} and Y_{tot} are the length and the width of the studied area. This equation is a parabola such that the four corners correspond to the respective heights of a, b, c and d, and such that the four edges are interpolated linearly. The center point of the rectangle also corresponds to the average of a, b, c and d.

The second step consists in filtering out the erroneous pixels from the coating topography. Indeed, a small part of the measured pixels does not reflect light because of the shape of the catalyst layer. An incorrect height it thus attributed to these pixels. These aberrant pixels are usually isolated and their height values are very different from those of the surrounding pixels. To correct the data, all aberrant pixels were corrected by applying a median filter of size 3 pixels × 3 pixels to every pixel: the median value among the 9 pixels forming a 3 pixels × 3 pixels square is attributed to the pixel located at its

center. Aberrant pixels are essentially present in the S_X85_7µm sample (Figure 15a). The detected very narrow peaks can be considered as erroneous because: (i) the width of these peaks is too low compared to the average size (7 µm) of the carbon xerogel particles used to prepare the layer and (ii) they systematically correspond to pixels of low reflected intensity. To illustrate the second issue, Figure 15b was obtained by removing the 10% of pixels with the lowest reflected light intensity from Figure 15a. A 5 pixels × 5 pixels median filter was applied to Figure 15a and eliminated all outliers while maintaining the shape integrity of the catalyst layer (Figure 15c). All the other samples were processed with a median filter 3 pixels × 3 pixels given the much lower occurrence of outliers.

3.4 Comparison of the results obtained by 3D laser scanning microscopy measurements on the different samples

Figure 16 compares the surface topography of samples F_XC72R, F_X85_0.5µm, S_XC72R and S_X85_7µm over a surface of 80 µm × 80 µm; the figures are those obtained after baseline correction and exclusion of erroneous pixels. The same height scale is used for the different samples and the proportions are respected according to the three axes. As shown from the profilometry measurements, the roughness of the layers obtained by film-casting is very low (Figures 16a and 16b). The roughness (~ 0.3 µm) of the sample prepared from the carbon xerogel ground at 0.5 µm (F_X85_0.5µm) is slightly higher and in fact reflects the size of the particles. In the case of layers obtained by spray-coating, the roughness is much more important, especially in the case of carbon xerogel with large particle sizes (S_X85_7µm, Figure 16d). As a matter of fact, while the average particle size is 7 µm, larger particles are also present (see distributions in ~~Supplementary Materials,~~ Figure 1), which can explain the presence of peaks of about 20 µm on the graph. Particles of about 7 µm are also present in the blue areas and are more clearly visible on the 2D projection of this sample topography in Figure 17.

3.5 Comparison of the profilometry and the 3D laser scanning microscopy measurements

The average values of the thickness and roughness of the deposits were calculated in the same way as in Section 3.1 (Equation 8) for samples F_XC72R, F_X85_0.5µm, S_XC72R and S_X85_7µm by processing the 3D microscopy images. The data are gathered in Table 2 and are compared to the values measured by profilometry. The thickness values obtained by 3D microscopy are not representative in the case of film-casting since, as shown in sections 3.1 and 3.2, the thickness is not homogeneous over the whole sample. As the 3D microscopy measurement is only performed on 0.25 cm^2 of deposit, the result highly depends on the sampling position, which could very well lead to

erroneous interpretations. Conversely, sprayed coatings are homogeneous, making 3D microscopy measurements more reliable and representative. In this case, it appears that the thicknesses determined by 3D microscopy are lower than those measured by contact profilometry. In the case of S_X85_7µm sample, the difference is about 30 %. The roughness values are similar for the two measurement techniques.

In order to compare the results of contact profilometry and 3D microscopy, a simulation of the passage of the profilometer tip (half-sphere of 12.5 µm) has been carried out on the 3D microscopy profile. The goal of the simulation is to check whether the bias due to the shape of the tip could explain the differences in the results as given by the two techniques. This simulation calculates the position a half-sphere of 12.5 µm radius can reach before it comes into contact with the 3D microscopy profile; afterwards, a new height which takes into account the shape of the tip is calculated. As mentioned earlier, the construction of the profile from a spherical tip is similar to the method developed by Lee *et al.* [46]. If the surface of the sample is smooth, the contact point is located at the basis of the hemisphere (Figure 7a). If the surface of the sample is rough, the point of contact depends on the tip environment (Figure 7b). The principle of calculation and the developed algorithm are detailed below.

Figure 18 illustrates the contact between the sphere and the profile for a given y coordinate, y_a. The center of the sphere is located at (x_a, y_a, z'). The objective of the algorithm is first to calculate, for each (x_a, y_a) coordinate pair of the 3D profile $z = p(x, y)$, the vertical position z' of the sphere in contact with profile $p(x, y)$.

To calculate the vertical position of the center of the sphere, z', the point of the profile p in contact with this sphere must be determined, and so, all points that may come into contact with the sphere of center (x_a, y_a, z') must be checked. All these points are located in a disk of radius r centered at (x_a, y_a); in Figure 18, they are comprised between $x_a - r$ and $x_a + r$. To find the contact point, a theoretical value of z' is calculated for each point of the profile p likely to come into contact with the sphere, *i.e.* all the points of the disk centered at (x_a, y_a). Among these values, the highest corresponds to a single point of contact between the sphere and the profile p.

The contact point of the sphere of radius r and of center (x_a, y_a, z') with a point of the profile p of coordinates (x, y, p (x, y)) (without taking into account the fact that the sphere may have crossed the profile p to reach this point of contact) can be expressed as:

$$(x - x_a)^2 + (y - y_a)^2 + (p(x, y) - z')^2 = r^2 \quad (10)$$

Then, the height of the sphere center, z', can be calculated from Eq. 10 as:

$$z' = p(x,y) + \sqrt{r^2 - (x - x_a)^2 - (y - y_a)^2} \quad (11)$$

The sphere of radius *r* and of coordinates (x_a, y_a, *z*') can *a priori* be in contact with all points of the profile *p* corresponding to a disk of radius *r* and center (x_a, y_a) (Equation 12). For all these points, the vertical positions *z*' of the sphere of coordinates (x_a, y_a, *z*') corresponding to a contact must be calculated (Equation 11). Then, among all these values, the contact point corresponding to a unique contact between the sphere and the profile *p* is the highest *z*' value.

$$(x - x_a)^2 + (y - y_a)^2 \leq r^2 \quad (12)$$

The simulated contact profilometer interprets each point of contact as it happens with the lower part of the sphere and not with its center. The radius of the sphere needs to be subtracted from *z*' in order to obtain the new vertical position *z*'' of the point A, simulating a measurement realized by a spherical contact profilometer of radius *r* (equation 13).

$$z'' = z' - r \quad (13)$$

In order to construct a 3D profile simulating entirely the passage of the profilometer tip on each pixel of the 3D microscopy profile, the above calculation has to be carried out for each pixel. The processing time being extremely long for each 3D profile, the calculations have been done on five lines equally spaced and not on the entire sample surface. For example, for a profile of 1100 pixels of width, the calculations are made on lines 200, 400, 600, 800 and 1000.

Figure 19 shows a portion of the 2D profiles extracted from the 3D microscopy measurements (in blue), and the simulation of the tip run (in red) for the four studied samples (F_XC72R, F_X85_0.5µm, S_XC72R and S_X85_7 µm). The profiles are comparable in all cases, except for the S_X85_7µm deposit. Indeed, in this case, the passage of the tip greatly overestimates the thickness of the layer and the details of the sample topography fade. Table 3 confirms these results by comparing the average thicknesses obtained by 3D microscopy and that calculated by simulation of tip motion onto the surface. Although the local values of thickness are not representative of the whole sample in the case of the film-casted coatings, the comparison is possible here since the same area is considered in both cases. These results confirm an overestimation of 45 % of the thickness in the case of carbon xerogel with 7 µm average particle size. Conversely, the surface state of S_XC72R causes a difference of 10 %, which remains quite acceptable. Table 3 also compares the average thickness calculated by simulation of the tip motion with the values obtained by profilometry measurements uncorrected for the tip geometry, as detailed in Section 3.1. This comparison is possible only in the case of deposits made by spray coating because layers prepared by film-casting require measurements on the entire sample to be representative of the average thickness. Indeed, it has been shown in sections 3.1 and 3.2 that the thickness of layers prepared by film-casting is not homogeneous as a function of the

position on the sample. For layers prepared by spray coating, the difference between the simulation and the actual profile is less than 10 % in both cases.

4 Conclusion

In this work, various carbon layers, mimicking the structure of catalyst layers for PEMFC applications, have been prepared by film-casting and spray-coating techniques. The aim was to study the surface topography of the resulting samples. Layers made of Nafion® and carbon, either Vulcan XC72® carbon black or carbon xerogel, were deposited on a Kapton® sheet.

The surface topography of the samples was characterized by contact profilometry and 3D laser scanning microscopy. The data obtained with both methods were processed to obtain accurate 3D representations of the surface of the layers. In both techniques, corrections due to the shape of the Kapton® support need to be taken into account. Moreover, for profilometry measurements, the overestimation of the thickness due to the size and the shape of the profilometer tip has been partially corrected. For 3D laser scanning microscopy, aberrant pixels due to low reflected light intensity were corrected using a median filter.

Contact profilometry allows to perform measurements over the entire surface of the sample. The results obtained from this technique show that layers produced by film-casting display very low roughness and a lower thickness at the edges of the coating. Note also that film-casting can lead to reproducibility issues, mainly due to the difficulty in controlling the solvent evaporation process. For layers prepared by spray-coating, the reproducibility and the homogeneity of the average thickness are improved; however, the surface is characterized by a higher roughness.

With 3D laser scanning microscopy measurements, only a small part of the sample was analyzed (0.25 cm^2) with a high definition, due to much longer observation times required. This 3D microscopy technique allows to characterize more accurately the surface topography; for example, large carbon xerogel particles (a few µm in size) could be observed individually. Overall, it has been shown that the measurements by 3D laser microscopy lead to lower, and thus more accurate, thickness values compared to contact profilometry, especially in the case of rough samples.

The simulation of the profilometer tip motion at the surface of the observed 3D microscopy profile explains the differences observed in terms of thickness between 3D microscopy and contact profilometry measurements. The contact profilometry measurements are generally reliable except when the roughness is very high: in the set of samples studied, the maximum observed overestimation reached 45 %. In this study, the 3D microscopy measurements proved more accurate, but not representative of the whole sample, especially for layers prepared by film-casting because

less-homogeneous over the whole sample. Nevertheless, stitching measurement is also an option for measuring the entire sample, even though sometimes prohibitive in terms of measurement time. Consequently, the use of lower magnification objectives would allow to measure the profile of larger surfaces within a reasonable time, and probably still with a better accuracy than contact profilometry.

All of these data finally clearly show that, depending on the coating technique and the carbon catalyst used, the topography of the resulting PEMFC layers can differ strongly. This in turn could have a high impact on the overall performance of the catalyst. The in-depth and complete characterization of the surface morphology of the layers is thus necessary. Techniques are available for that, but, as shown in the present study, the results have to be post-processed to account for the limitations of each technique, which are the tip footprint for contact profilometry and the reflectivity defect for 3D laser microscopy.

Author Contribution statement

Fabien L. Deschamps : Conceptualization; Data curation; Formal analysis; Investigation; Methodology; Visualization; Software; Writing - original draft; Writing - review & editing

Julien G. Mahy : Data curation; Formal analysis; Investigation; Visualization; Writing - original draft; Writing - review & editing

Alexandre F. Léonard : Data curation; Methodology; Roles/Writing - original draft; Writing - review & editing

Stéphanie D. Lambert : Data curation; Project administration; Resources; Writing - original draft

Adrien Dewandre : Data curation; Formal analysis; Investigation; Writing - original draft

Benoît Scheid : Data curation; Formal analysis; Investigation; Methodology; Writing - original draft

Nathalie Job : Conceptualization; Data curation; Formal analysis; Funding acquisition; Investigation; Methodology; Project administration; Resources; Supervision; Validation; Visualization; Writing - original draft; Writing - review & editing

Acknowledgements

F. Deschamps and S. D. Lambert are grateful to the Belgian F.R.S.-FNRS for a FRIA fellowship grant and a Senior Research Associate position respectively. A. Léonard and N. Job thank the financial support from the Région Wallonne (BATWAL, grant agreement 1318146, PE Plan Marshall 2.vert; HYLIFE, grant agreement 1410135) and the Research Funds for Coal and Steel - RFCS (PROMOTEE, grant agreement 709741). The authors also thank the University of Liège (Fonds Spéciaux pour la

Recherche FSR C13/09) and the Fonds de Bay for their financial support. B.S. and A.D. thanks the Walloon Region for the financial support for the 3D laser microscope through the MecaTech-Legomedic project. B.S. thanks the F.R.S.-FNRS for financial support.

Compliance with ethical standards

Conflict of interest: The authors declare that they have no conflicts of interest.

Data availability

The raw/processed data required to reproduce these findings cannot be shared at this time as the data also forms part of an ongoing study.

References

[1] N. Guerrero Moreno, M. Cisneros Molina, D. Gervasio, J.F. Pérez Robles, Approaches to polymer electrolyte membrane fuel cells (PEMFCs) and their cost, Renew. Sustain. Energy Rev. 52 (2015) 897–906. doi:10.1016/j.rser.2015.07.157.

[2] O.Z. Sharaf, M.F. Orhan, An overview of fuel cell technology: Fundamentals and applications, Renew. Sustain. Energy Rev. 32 (2014) 810–853. doi:10.1016/j.rser.2014.01.012.

[3] P.-Y. Olu, A. Zadick, N. Job, M. Chatenet. Anode (electro)catalysts for direct borohydride and ammonia borane fuel cells. In: Electrocatalysts for low temperature fuel cells. Fundamental and recent trends, T. Maiyalagan, S. Viswanathan (Eds.), Wiley-VCH, Weinheim, Germany, 2017, pp. 317-346.

[4] H.S. Park, Y.H. Cho, Y.H. Cho, C.R. Jung, J.H. Jang, Y.E. Sung, Performance enhancement of PEMFC through temperature control in catalyst layer fabrication, Electrochim. Acta 53 (2007) 763–767. doi:10.1016/j.electacta.2007.07.046.

[5] P.K. Shen, PEM Fuel Cell Catalyst Layers and MEAs, in: PEM Fuel Cell Electrocatalysts and Catalyst Layers: Fundamentals and Applications, J. Zhang (Ed.), Springer London, London, 2008: pp. 355–380. doi:10.1007/978-1-84800-936-3_7.

[6] A. Zubiaur, N. Job, Streamlining of the synthesis process of Pt / carbon xerogel electrocatalysts with high Pt loading for the oxygen reduction reaction in proton exchange membrane fuel cells applications, Appl. Catal. B Environ. 225 (2018) 364–378.

doi:10.1016/j.apcatb.2017.11.059.

[7] H.A. Gasteiger, S.S. Kocha, B. Sompalli, F.T. Wagner, Activity benchmarks and requirements for Pt , Pt-alloy , and non-Pt oxygen reduction catalysts for PEMFCs, Appl. Catal. B Environ. 56 (2005) 9–35. doi:10.1016/j.apcatb.2004.06.021.

[8] E. Antolini, Formation, microstructural characteristics and stability of carbon supported platinum catalysts for low temperature fuel cells, J. Mater. Sci. 38 (2003) 2995–3005. doi:10.1023/A:1024771618027.

[9] J. Stacy, Y.N. Regmi, B. Leonard, M. Fan, The recent progress and future of oxygen reduction reaction catalysis: A review, Renew. Sustain. Energy Rev. 69 (2017) 401–414. doi:10.1016/j.rser.2016.09.135.

[10] F. Maillard, P.A. Simonov, E.R. Savinova, Carbon Materials as Supports for Fuel Cell Electrocatalysts, in: P. Serp, J.L. Figueiredo (Eds.), Carbon Mater. Catal., Wiley-VCH, 2009: pp. 429–480.

[11] S. Sharma, B.G. Pollet, Support materials for PEMFC and DMFC electrocatalysts — A review, J. Power Sources 208 (2012) 96–119. doi:10.1016/j.jpowsour.2012.02.011.

[12] D. Banham, F. Feng, T. Fürstenhaupt, K. Pei, S. Ye, V. Birss, Novel Mesoporous Carbon Supports for PEMFC Catalysts, Catalysts 15 (2015) 1046–1067. doi:10.3390/catal5031046.

[13] S. Shahgaldi, J. Hamelin, Improved carbon nanostructures as a novel catalyst support in the cathode side of PEMFC : a critical review, Carbon 94 (2015) 705–728. doi:10.1016/j.carbon.2015.07.055.

[14] F. Maillard, N. Job, M. Chatenet, Approaches to Synthesize Carbon-Supported Platinum-Based Electrocatalysts for Proton-Exchange Membrane Fuel Cells, Chap. 14 in: New Future Developments in Catalysis. Batteries, Hydrogen Storage and Fuel Cells, S.L. Suib (Ed.) , Elsevier B.V., 2013: pp. 407–428. doi:10.1016/B978-0-444-53880-2.00019-3.

[15] N. Job, B. Heinrichs, S.D. Lambert, J. Pirard, J.F. Colomer, B. Vertruyen, J. Marien, Carbon Xerogels as Catalyst Supports : Study of Mass Transfer, AIChE J. 52 (2006). doi:10.1002/aic.

[16] N. Job, J. Marie, S. Lambert, S. Berthon-Fabry, P. Achard, Carbon xerogels as catalyst supports for PEM fuel cell cathode, Energy Convers. Manag. 49 (2008) 2461–2470. doi:10.1016/j.enconman.2008.03.025.

[17] J. Marie, R. Chenitz, M. Chatenet, S. Berthon-Fabry, N. Cornet, P. Achard, Highly porous PEM fuel cell cathodes based on low density carbon aerogels as Pt-support: Experimental study of

the mass-transport losses, J. Power Sources 190 (2009) 423–434. doi:10.1016/j.jpowsour.2009.01.047.

[18] A. Suzuki, U. Sen, T. Hattori, R. Miura, R. Nagumo, H. Tsuboi, N. Hatakeyama, A. Endou, H. Takaba, M.C. Williams, A. Miyamoto, IIonomer content in the catalyst layer of polymer electrolyte membrane fuel cell (PEMFC): Effects on diffusion and performance, Int. J. Hydrogen Energy 36 (2011) 2221–2229. doi:10.1016/j.ijhydene.2010.11.076.

[19] G. Sasikumar, J.W. Ihm, H. Ryu, Dependence of optimum Nafion content in catalyst layer on platinum loading, J. Power Sources 132 (2004) 11–17. doi:10.1016/j.jpowsour.2003.12.060.

[20] S.S. Kocha, Principles of MEA preparation, in: Handbook Fuel Cells-Fundamentals Technology and Applications, W. Vielstich, A. Lamm, H.A. Gasteiger, H. Yokokawa (Eds.), John Wiley and Sons, 2003: pp. 538–565. Doi:10.1002/9780470974001.f303047.

[21] R.R. Passos, V.A. Paganin, E.A. Ticianelli, Studies of the performance of PEM fuel cell cathodes with the catalyst layer directly applied on Nafion membranes, Electrochim. Acta 51 (2006) 5239–5245. doi:10.1016/j.electacta.2006.01.044.

[22] B. Millington, S. Du, B.G. Pollet, The effect of materials on proton exchange membrane fuel cell electrode performance, J. Power Sources 196 (2011) 9013–9017. doi:10.1016/j.jpowsour.2010.12.043.

[23] S. Jeon, J. Lee, G.M. Rios, H.J. Kim, S.Y. Lee, E. Cho, T.H. Lim, J. Hyun Jang, Effect of ionomer content and relative humidity on polymer electrolyte membrane fuel cell (PEMFC) performance of membrane-electrode assemblies (MEAs) prepared by decal transfer method, Int. J. Hydrogen Energy 35 (2010) 9678–9686. doi:10.1016/j.ijhydene.2010.06.044.

[24] J. Wee, K. Lee, S.H. Kim, Fabrication methods for low-Pt-loading electrocatalysts in proton exchange membrane fuel cell systems, J. Power Sources 165 (2007) 667–677. doi:10.1016/j.jpowsour.2006.12.051.

[25] A.T. Haug, R.E. White, J.W. Weidner, W. Huang, S. Shi, T. Stoner, N. Rana, Increasing Proton Exchange Membrane Fuel Cell Catalyst Effectiveness Through Sputter Deposition, J. Electrochem. Soc. 149 (2002) A280. doi:10.1149/1.1446082.

[26] E.J. Taylor, E.B. Anderson, N.R.K. Vilambi, Preparation of High-Platinum-Utilization Gas Diffusion Electrodes for Proton-Exchange-Membrane Fuel Cells, J. Electrochem. Soc. 139 (1992) L45. doi:10.1149/1.2069439.

[27] M. Ahn, Y. Cho, N. Jung, J.W. Lim, Y.S. Kang, Y. Sung, Structural Modification of a Membrane Electrode Assembly via a Spray Coating in PEMFCs, J. Electrochem. Soc. 159 (2012) 145–149.

doi:10.1149/2.011202jes.

[28] G. Bender, T.A. Zawodzinski, A.P. Saab, Fabrication of high precision PEFC membrane electrode assemblies, J. Power Sources 124 (2003) 114–117. doi:10.1016/S0378-7753(03)00735-3.

[29] S. Escribano, P. Aldebert, Iowcs Electrodes for hydrogen / oxygen polymer electrolyte membrane fuel cells, Solid State Ionics 77 (1995) 318–323.

[30] I. Park, W. Li, A. Manthiram, Fabrication of catalyst-coated membrane-electrode assemblies by doctor blade method and their performance in fuel cells, J. Power Sources 195 (2010) 7078–7082. doi:10.1016/j.jpowsour.2010.05.004.

[31] B. Koraishy, J.P. Meyers, K.L. Wood, Manufacturing of membrane electrode assemblies for fuel cells, In: International conference on manufacturing research (IMCR) 2009 1–13. https://pdfs.semanticscholar.org/fc3d/c1538c2eafd0ea27df7b930cd13613869f05.pdf (accessed 15 November 2019).

[32] B. Millington, V. Whipple, B.G. Pollet, A novel method for preparing proton exchange membrane fuel cell electrodes by the ultrasonic-spray technique, J. Power Sources 196 (2012) 8500–8508. doi:10.1016/j.jpowsour.2011.06.024.

[33] H. Yu, J.M. Roller, S. Kim, Y. Wang, D. Kwak, R. Maric, One-Step Deposition of Catalyst Layers for High Temperature Proton Exchange Membrane Fuel Cells (PEMFC), J. Electrochem. Soc. 161 (2014) 622–627. doi:10.1149/2.045405jes.

[34] Y.C. Lai, K.L. Huang, C.H. Tsai, W.J. Lee, Y.L. Chen, Sputtered Pt loadings of membrane electrode assemblies in proton exchange membrane fuel cells, Int. J. Energy Res. (2012) 918–927. doi:10.1002/er.

[35] A.M. Chaparro, R. Ben, L. Gubler, G.G. Scherer, L. Daza, Study of membrane electrode assemblies for PEMFC , with cathodes prepared by the electrospray method, J. Power Sources 169 (2007) 77–84. doi:10.1016/j.jpowsour.2007.01.044.

[36] T. Huang, H. Shen, T. Jao, F. Weng, A. Su, Ultra-low Pt loading for proton exchange membrane fuel cells by catalyst coating technique with ultrasonic spray coating machine, Int. J. Hydrogen Energy 7 (2012) 7–14. doi:10.1016/j.ijhydene.2012.04.108.

[37] M. Prasanna, E.A. Cho, T.H. Lim, I.H. Oh, Effects of MEA fabrication method on durability of polymer electrolyte membrane fuel cells, Electrochim. Acta 53 (2008) 5434–5441. doi:10.1016/j.electacta.2008.02.068.

[38] F. Mack, M. Klages, J. Scholta, L. Jörissen, T. Morawietz, R. Hiesgen, D. Kramer, R. Zeis, Morphology studies on high-temperature polymer electrolyte membrane fuel cell electrodes, J. Power Sources 255 (2014) 431–438. doi:10.1016/j.jpowsour.2014.01.032.

[39] S. Malik, L. Smith, J. Sharman, E.M. Holt, S.P. Rigby, Pore Structural Characterization of Fuel Cell Layers Using Integrated, Ind. Eng. Chem. Res. 55 (2016) 10850-10859. doi:10.1021/acs.iecr.6b01617.

[40] N. Job, A. Théry, R. Pirard, J. Marien, L. Kocon, J.N. Rouzaud, F. Béguin, J.P. Pirard, Carbon aerogels , cryogels and xerogels : Influence of the drying method on the textural properties of porous carbon materials, Carbon 43 (2005) 2481–2494. doi:10.1016/j.carbon.2005.04.031.

[41] M.-L.C. Piedboeuf, A.F. Léonard, K. Traina, N. Job, Influence of the textural parameters of resorcinol – formaldehyde dry polymers and carbon xerogels on particle sizes upon mechanical milling, Colloids Surfaces A Physicochem. Eng. Asp. 471 (2015) 124–132. doi:10.1016/j.colsurfa.2015.02.014.

[42] N. Job, R. Pirard, J. Marien, J.P. Pirard, Porous carbon xerogels with texture tailored by pH control during sol-gel process, Carbon 42 (2004) 619–628. doi:10.1016/j.carbon.2003.12.072.

[43] F. Chevallier, L. Aymard, J. Tarascon, Influence of Oxygen and Hydrogen Milling Atmospheres on the Electrochemical Properties of Ballmilled Graphite, J. Electrochem. Soc. 148 (2001) 1216–1224. doi:10.1149/1.1405800.

[44] J.S. Villarrubia, Algorithms for scanned probe microscope image simulation, surface reconstruction, and tip estimation, J. Res. Natl. Inst. Stand. Technol. 102 (1997) 425–454. doi:10.6028/jres.102.030.

[45] W.R. DeVries, C.-J. Li, Algorithms to Deconvolve Stylus Geometry From Surface Profile Measurements, J. Eng. Ind. 107 (1985) 167–174. doi:10.1115/1.3185981.

[46] D.H. Lee, 3-Dimensional profile distortion measured by stylus type surface profilometer, Measurement 46 (2013) 803–814. doi:10.1016/j.measurement.2012.09.022.

Figure captions:

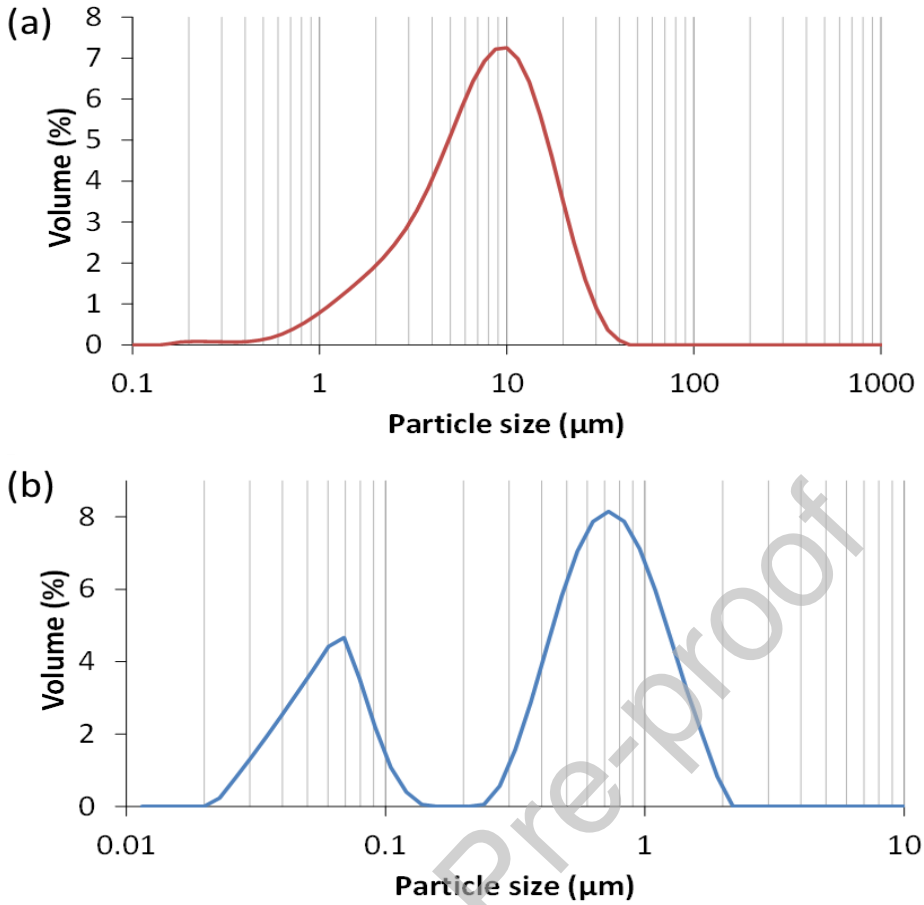

Figure 1: Particle size distribution for the carbon xerogel sample after (a) dry grinding (mean particle size ~7 µm) and (b) liquid grinding (mean particle size = 0.5 µm).

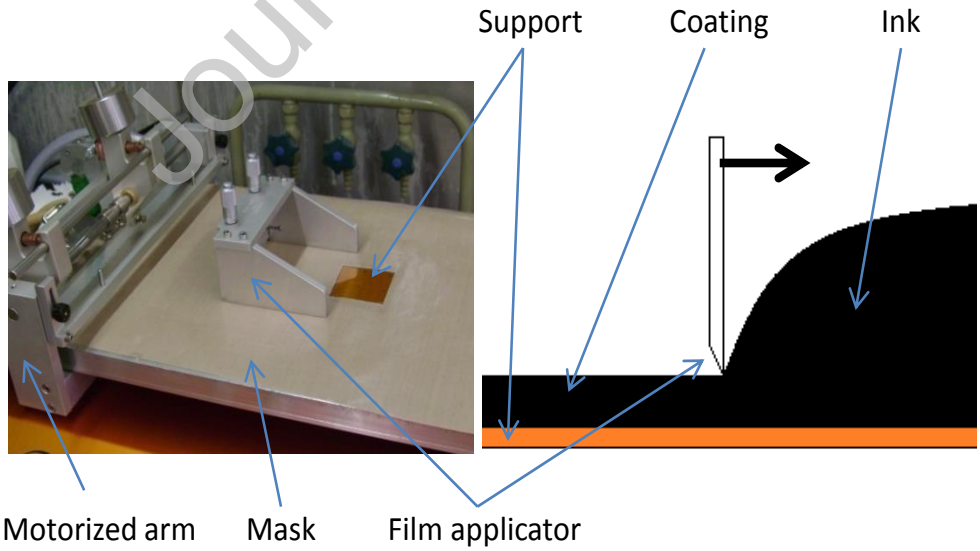

Figure 2: Picture and scheme of the film-casting device.

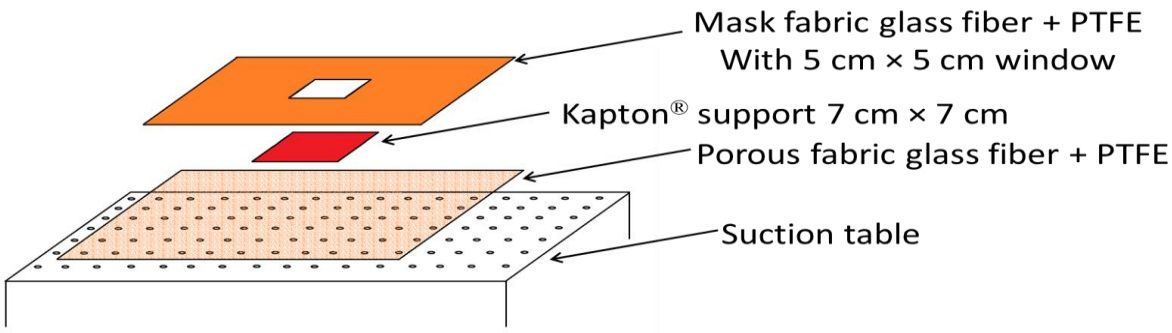

Figure 3: Scheme of the sample set-up for film-casting.

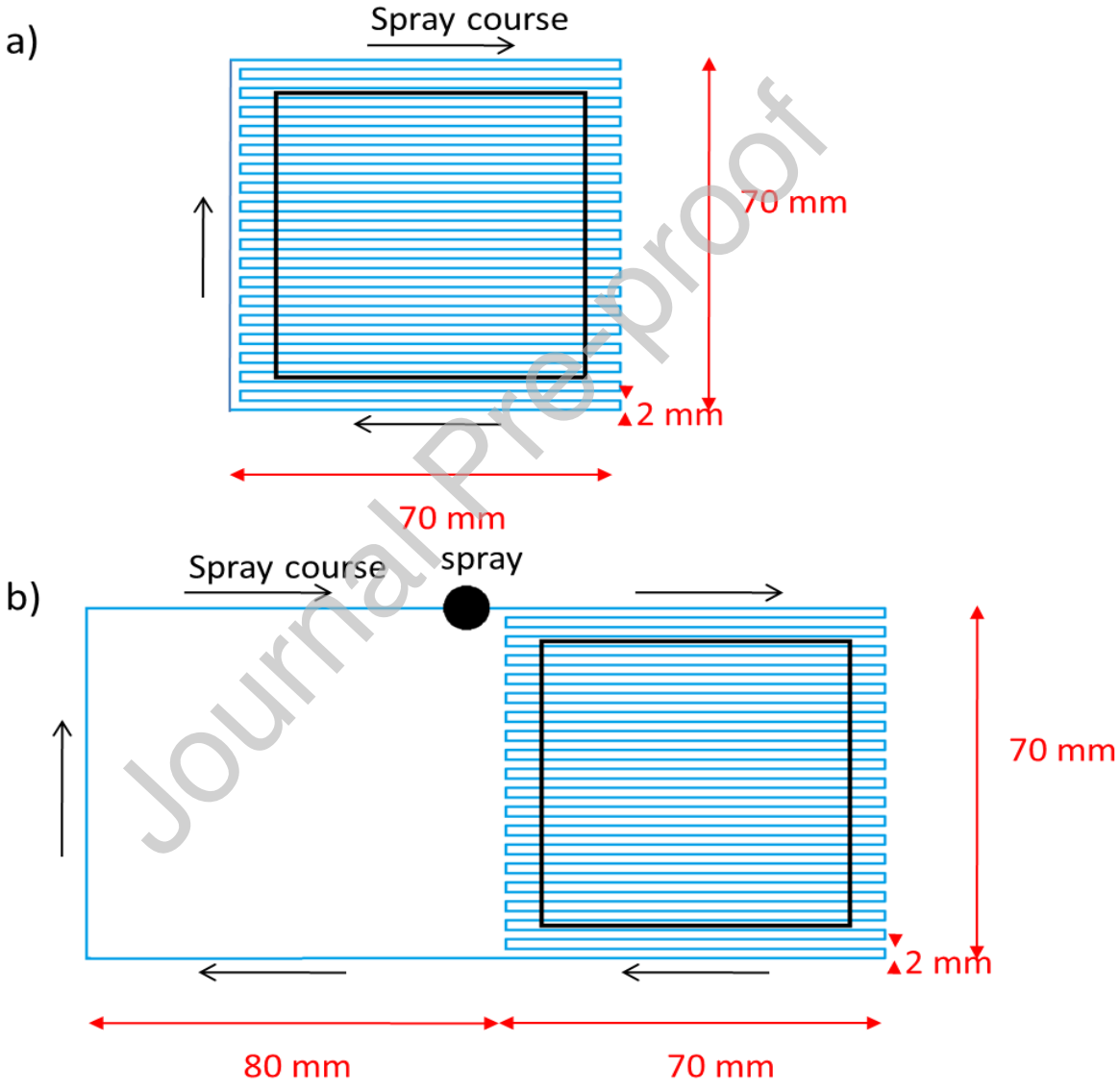

Figure 4: (a) Scheme of spray course without spacing at the return of the nozzle and (b) scheme of spray course used for all spray-coatings.

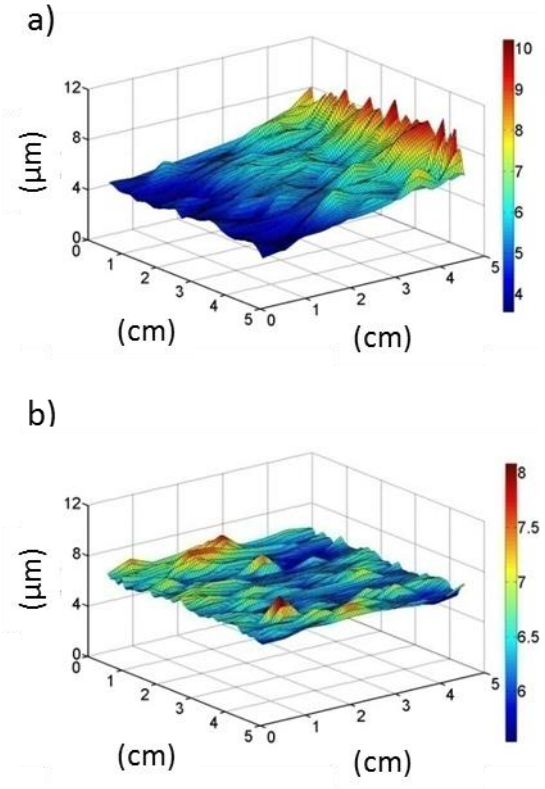

Figure 5: 3D Profiles of S_XC72R sample with: (a) Figure 4a course and (b) Figure 4b course. (For the correct interpretation of the colors, the reader is referred to the web version of this article.)

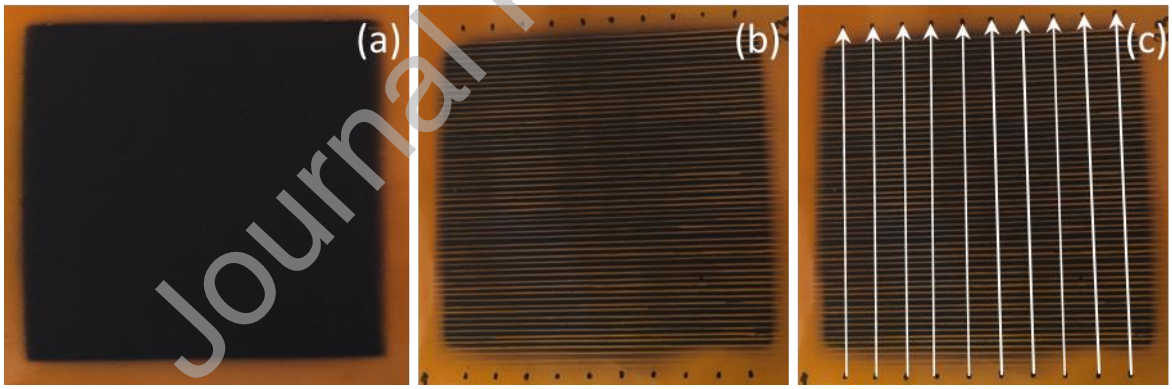

Figure 6: Preparation of the catalytic layers coated on Kapton® for profilometry measurements; (a) layer before preparation, (b) layer after removing 250 µm strips, spaced 1 mm apart, (c) profilometry measurements on one sample (blue arrows).

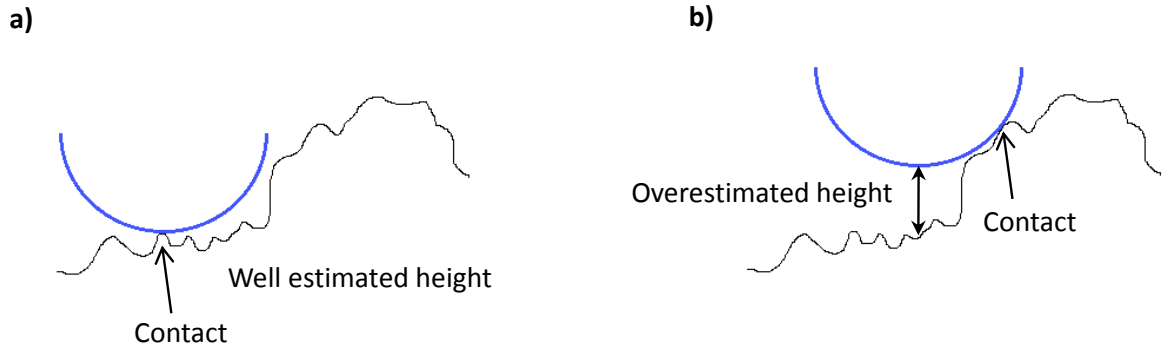

Figure 7: Height estimation during profilometry measurement: (a) contact between the sample and the middle of the tip, (b) contact between the sample and the edge of the tip. The blue half-circle corresponds to the tip surface.

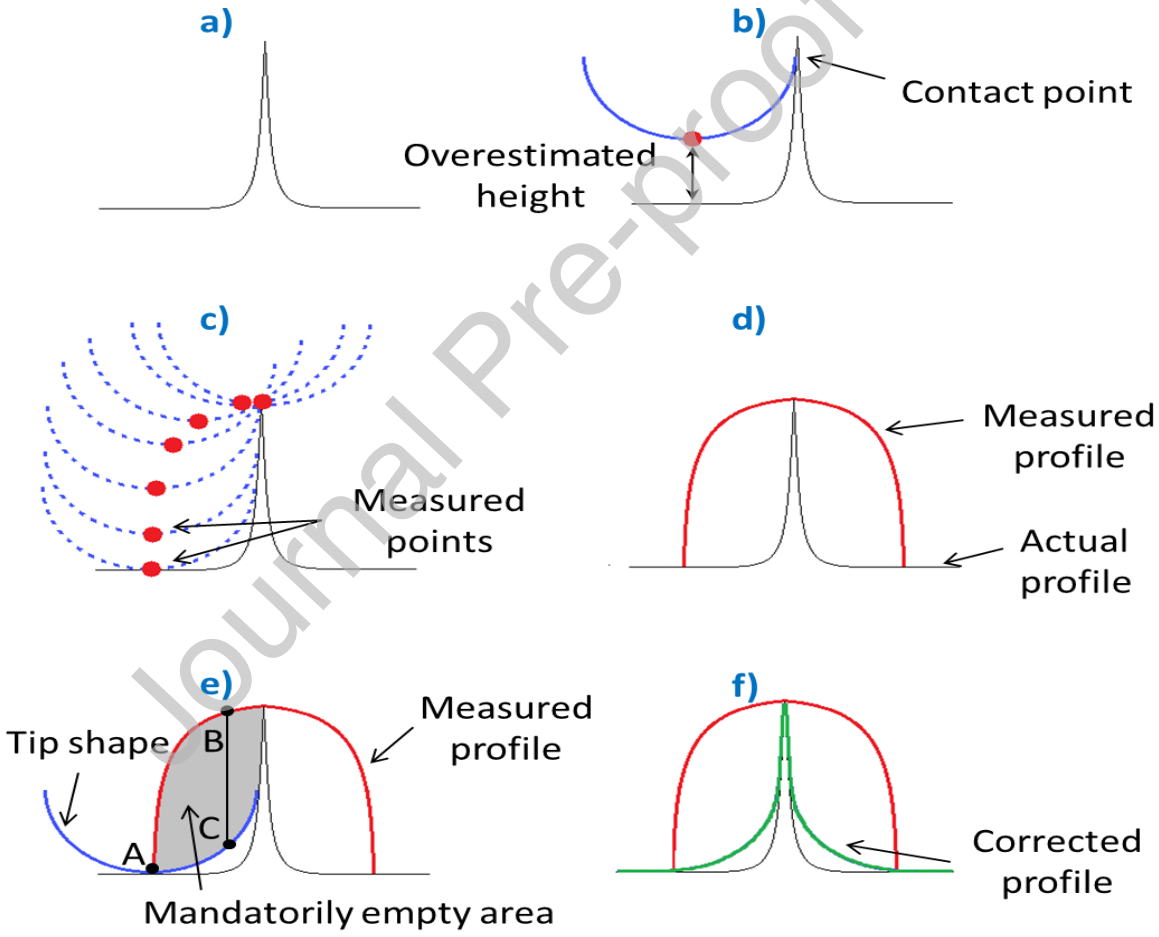

Figure 8: Correction of the profilometry measurements: (a) actual sample profile, (b) example of tip position leading to height overestimation during measurement, (c) tip motion on the sample, (d) raw profile response from the profilometer, (e) detection of overestimated height points, (f) corrected profile.

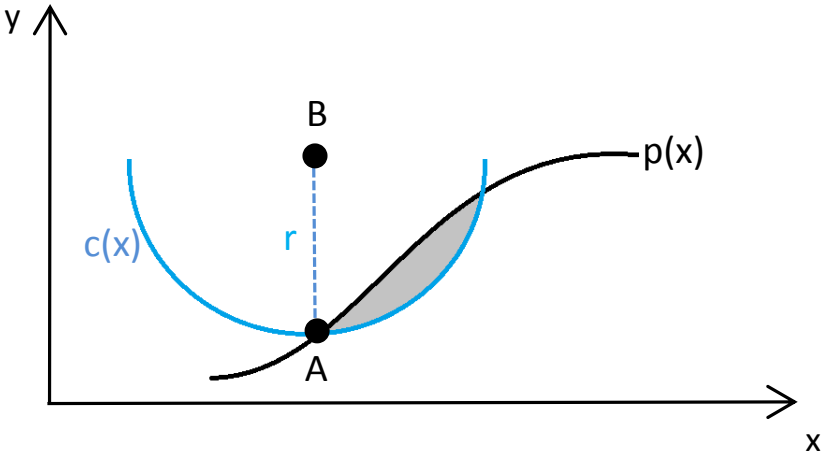

Figure 9: Scheme explaining the calculations concerning the impact of the profilometer tip shape (in blue) on the measured profile (in black). C(x) represents the profilometer tip, p(x) the measured profile obtained by profilometry, A is a point of the profile and B is the center of the tip.

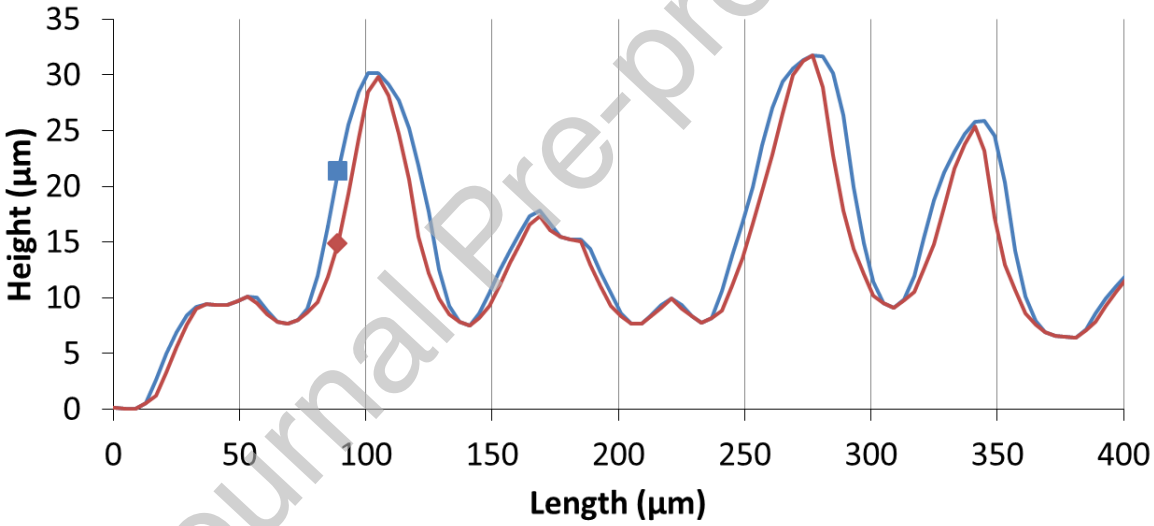

Figure 10: Comparison of profilometer signal: (■) before correction, (◆) after correction of the tip shape.

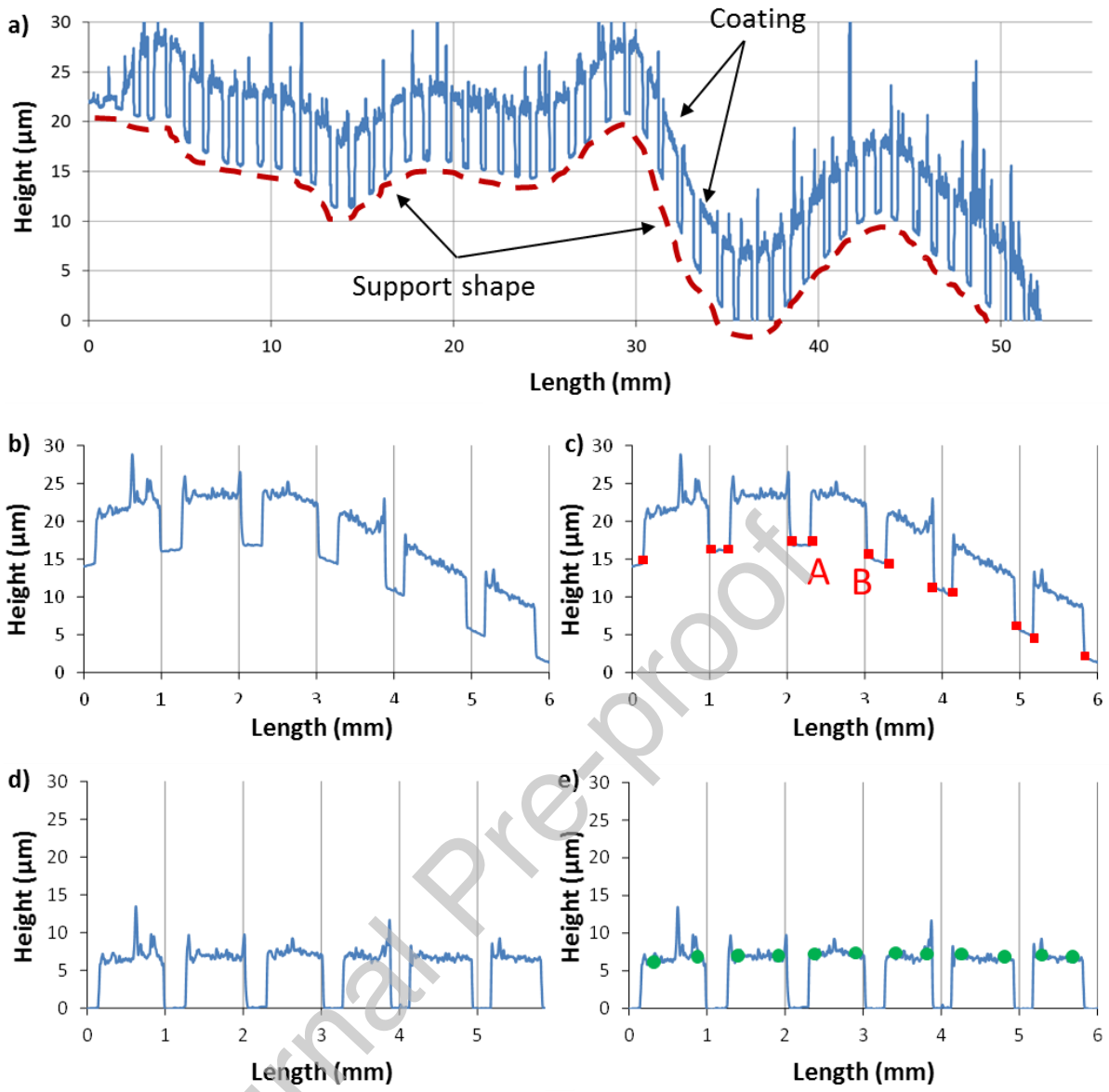

Figure 11: (a) Example of profilometry measurement and profile correction over a length of 6 mm: (b) signal after correction of the tip shape, (c) selection of zones without coating for processing, (d) subtraction of the substrate shape, and (e) selection of zones with coating. Sample S_XC72R.

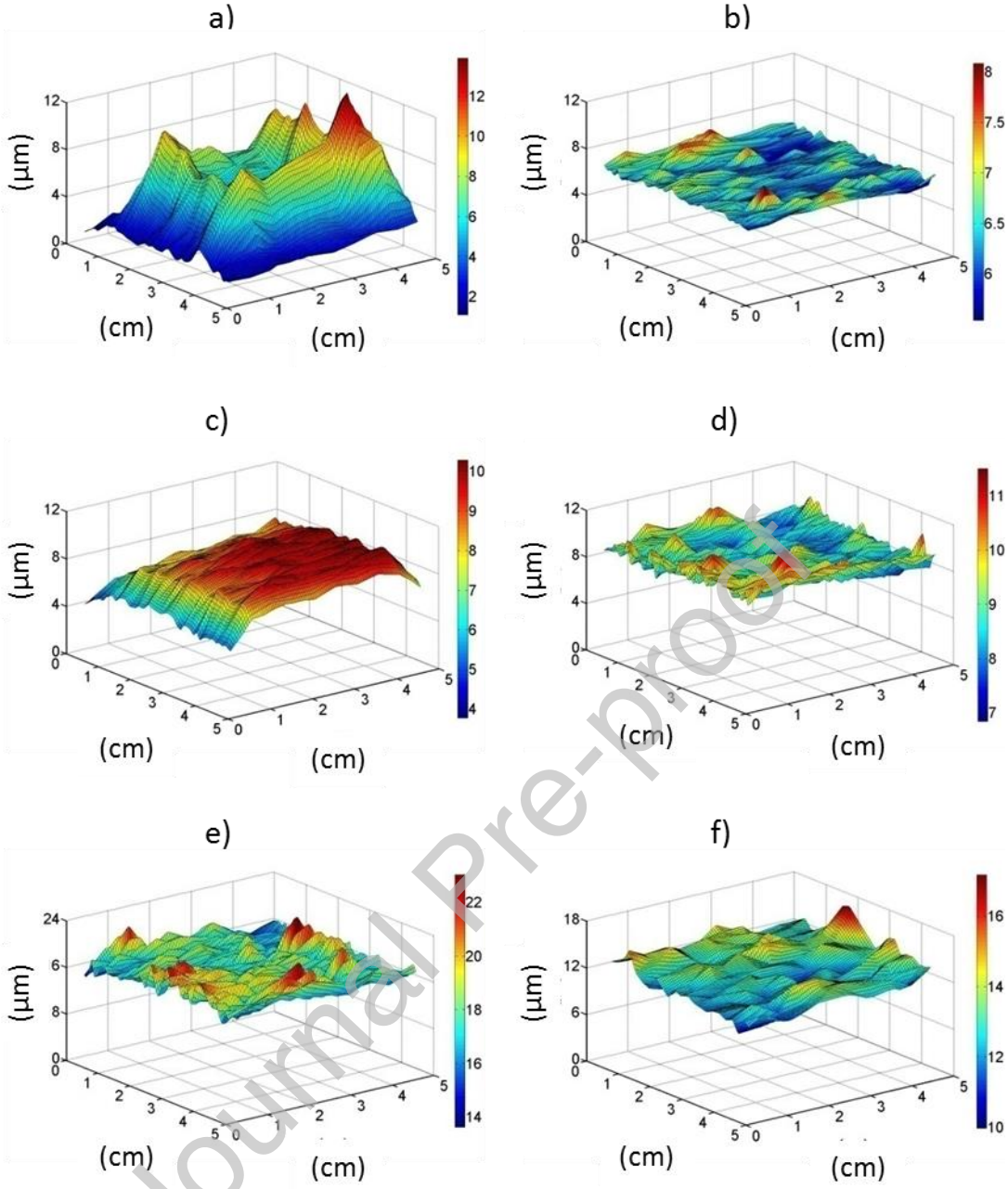

Figure 12: Comparison of 3D profiles depending on the coating technique and on the used carbon in the catalyst layer: (a) F_XC72R; (b) S_XC72R; (c) F_X85_0.5µm; (d) S_X85_0.5µm_A; (e) S_X85_0.5µm_B and (f) S_X85_7µm. The color legend is adapted for each sample. (For the correct interpretation of the colors, the reader is referred to the web version of this article.)

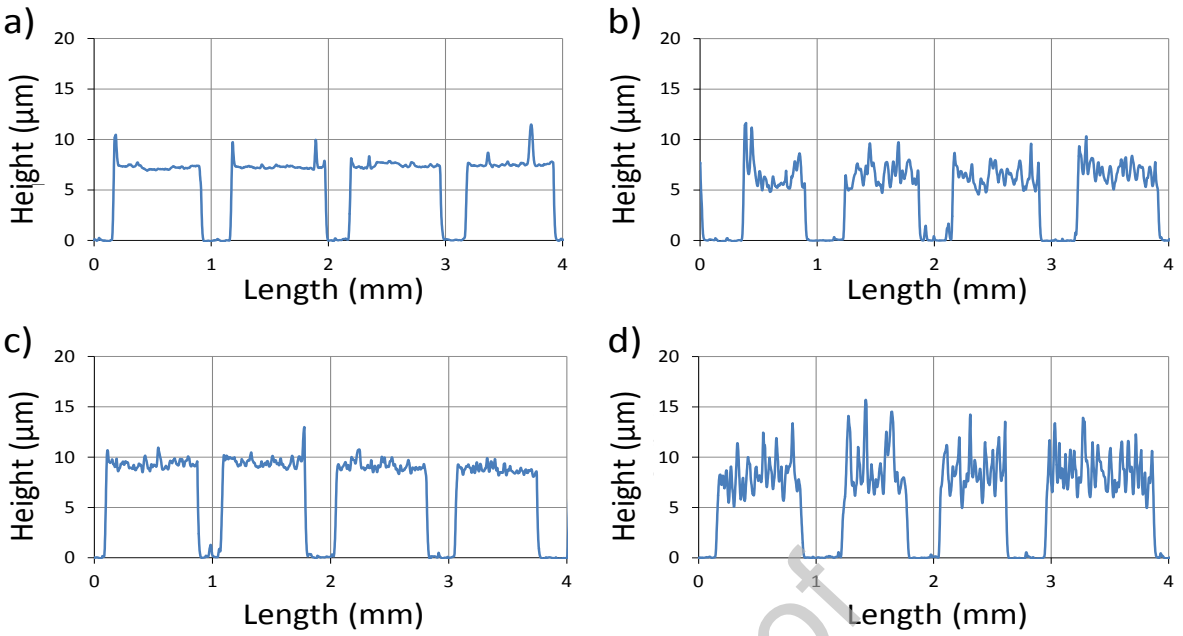

Figure 13: Comparison of a 4 mm portion of 2D profiles: (a) F_XC72R; (b) S_XC72R; (c) F_X85_0.5µm and (d) S_X85_0.5µm_A.

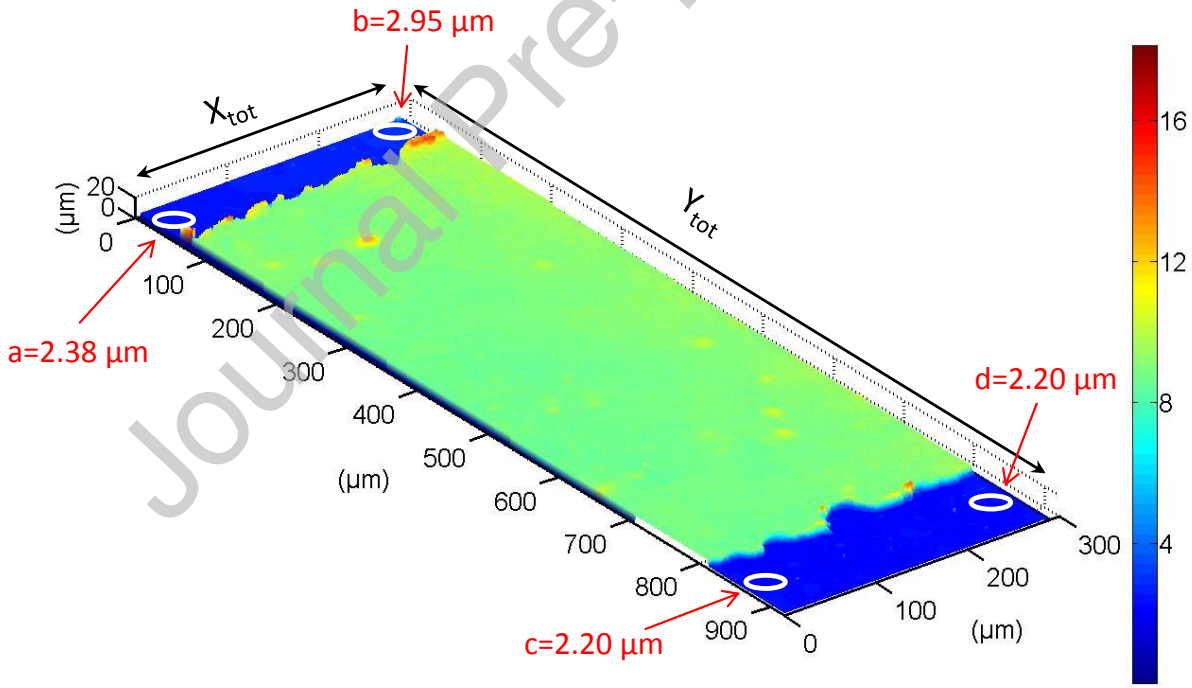

Figure 14: 3D laser scanning micrograph of sample F_XC72R before any correction. The blue areas correspond to the support and the green area to the coating. a, b, c and d values are the height of the support at the four corners of the 3D profile.

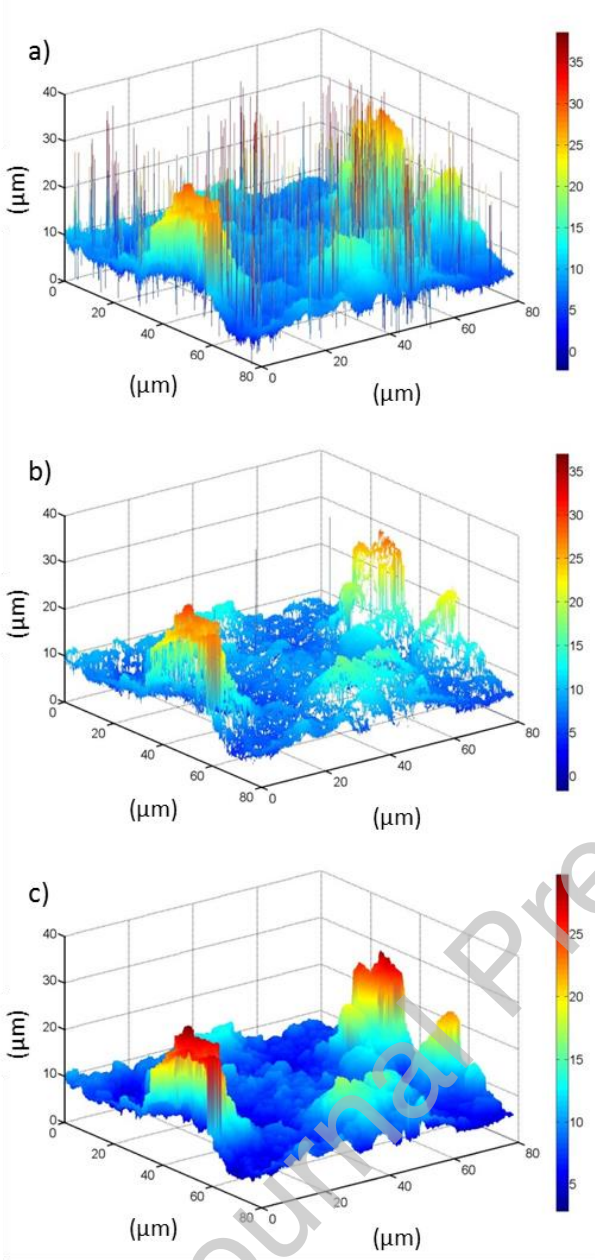

Figure 15: 3D laser scanning micrograph of sample S_X85_7µm (a) before any correction, (b) after removal of the 10 % of pixels presenting the lowest reflected light intensity and (c) after correction by a 5 × 5 median filter. The color legend is adapted for each sample. (For the correct interpretation of the colors, the reader is referred to the web version of this article.)

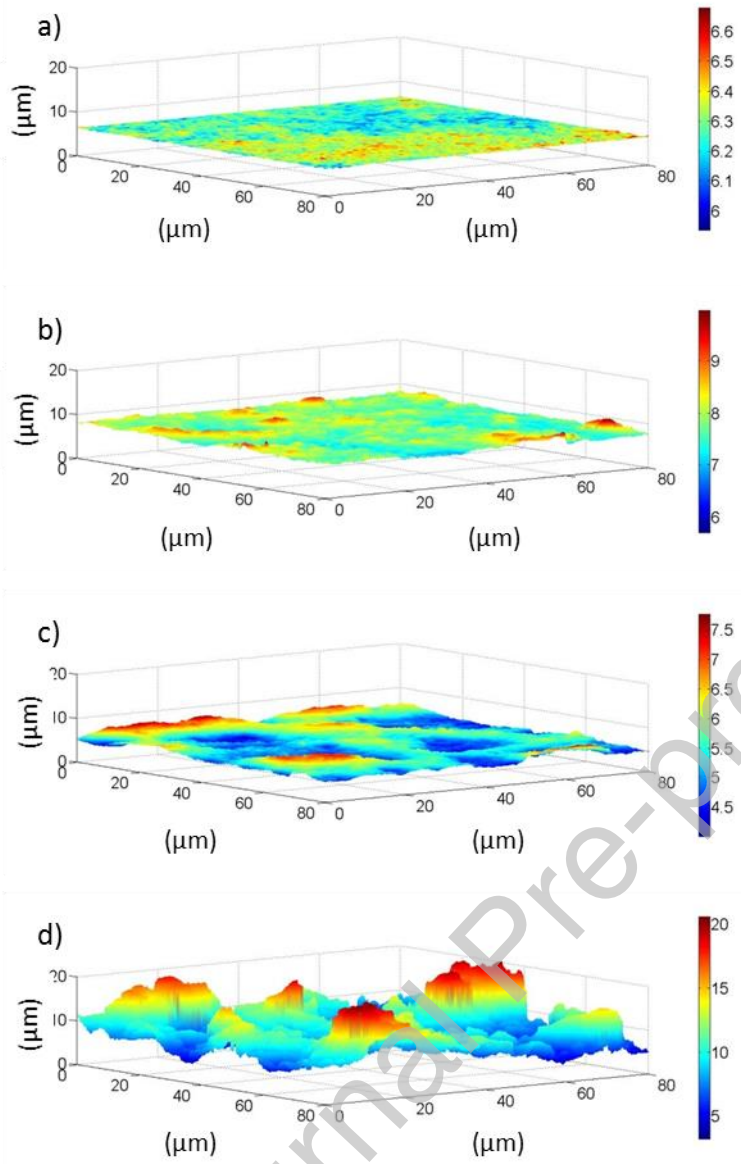

Figure 16: Comparison of 3D profiles obtained by 3D laser scanning microscopy: (a) F_XC72R, (b) F_X85_0.5µm, (c) S_XC72R and (d) S_X85_7µm samples. The color legend is adapted for each sample. (For the correct interpretation of the colors, the reader is referred to the web version of this article.)

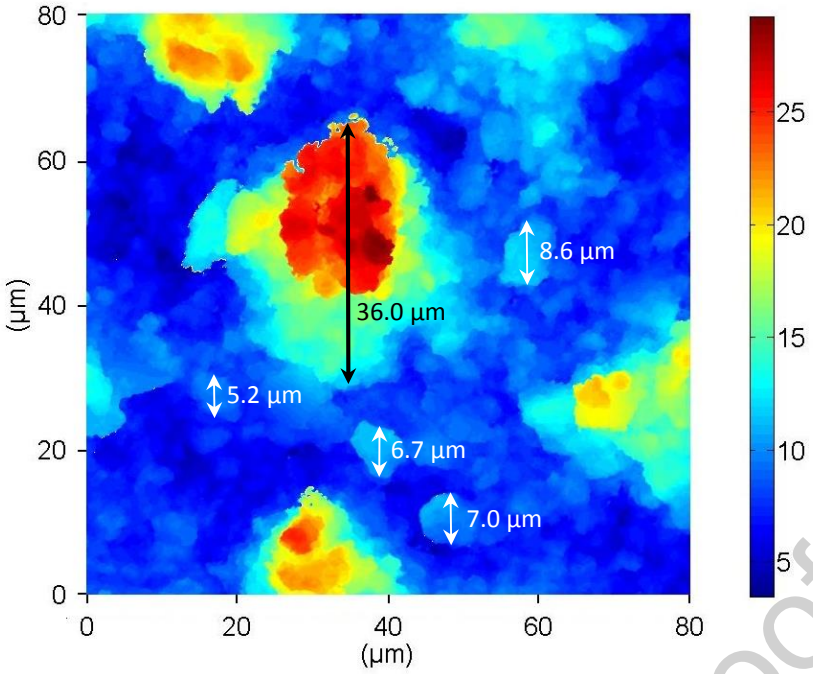

Figure 17: 2D projection of the 3D topography profile obtained by 3D laser scanning microscopy of sample S_X85_7µm (Figure 16d and 17 do not represent the same region of the sample).

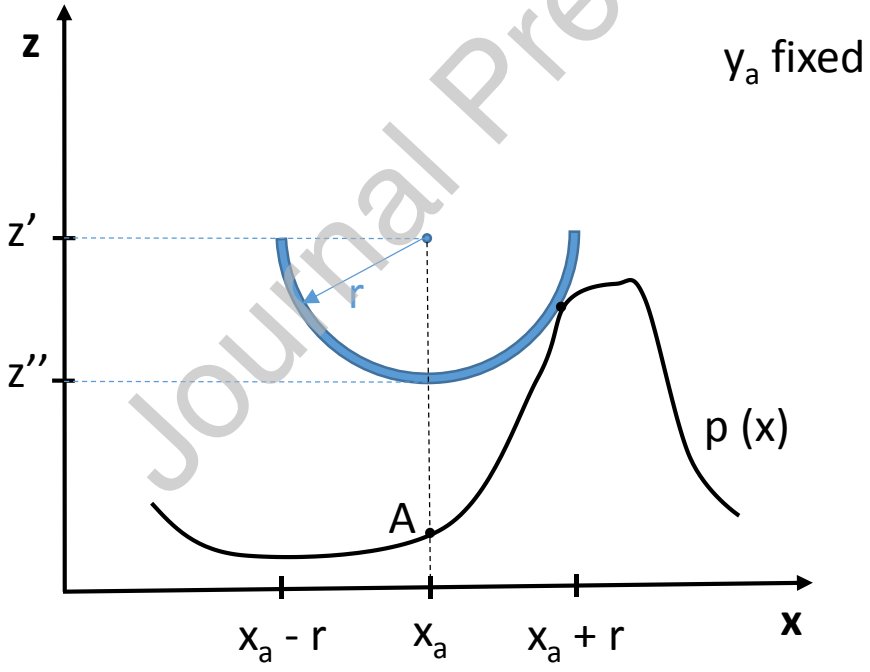

Figure 18: Representation of the calculation of the profilometry profile corresponding to the laser microscopy profile $p(x)$. The blue half-circle corresponds to the simulated tip shape. y_a is fixed.

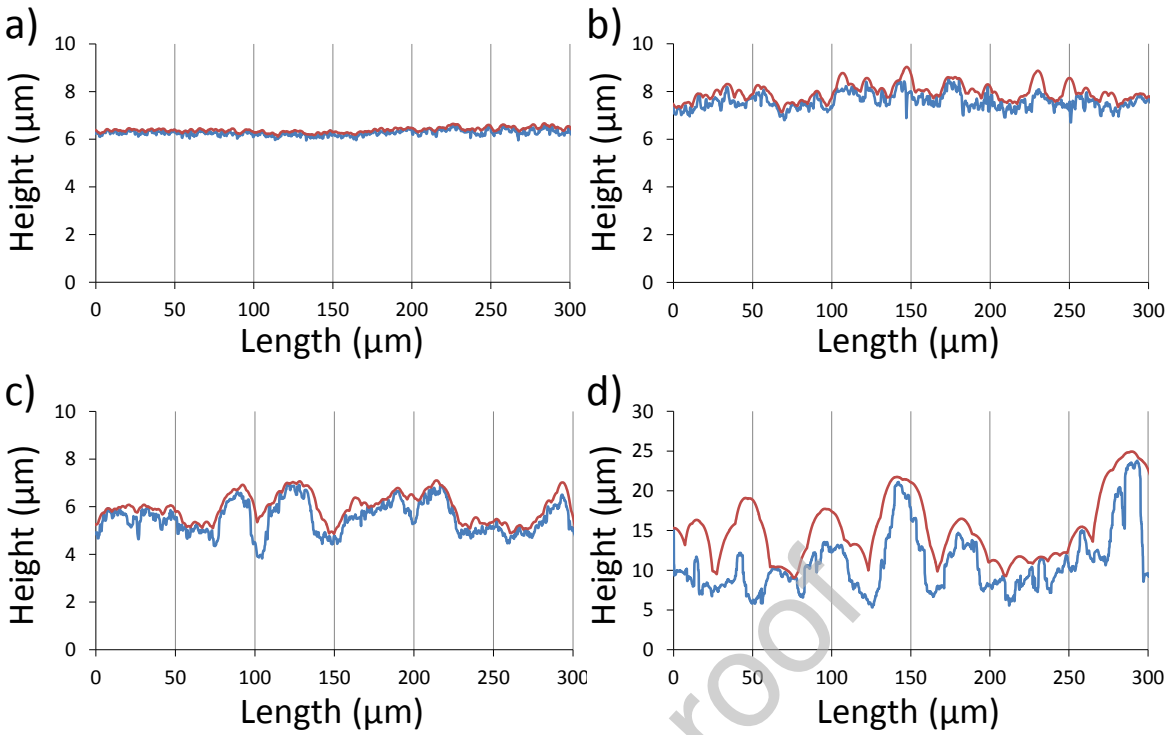

Figure 19: 2D portion of a 3D laser scanning microscopy profile (in blue), and simulation of the profile obtained by the motion of a hemispherical tip (radius of 12.5 µm) on the blue curve (in red): (a) F_XC72R, (b) F_X85_0.5µm, (c) S_XC72R and (d) S_X85_7µm.

Table captions:

Table 1: Composition of the inks, deposition procedure and mass of the coatings.

Table 2: Thickness, roughness and density measured by profilometry or 3D laser scanning microscopy.

Table 3: Comparison of the mean thickness obtained by simulating the motion of the profilometer tip on the 3D microscopy profile with the experimental 3D microscopy and profilometry measurements.

Table 1: Composition of the inks, deposition procedure and mass of the coatings.

	Type of coating	Type of carbon	Carbon	Nafion® solution 15 wt.%	Nafion® solution 20 wt.%	Water	Isopropanol	Number of passes	Mass
	(-)	(-)	(wt.%)	(wt.%)	(wt.%)	(wt.%)	(wt.%)	(-)	(mg)
			± 1 %	± 1 %	± 1 %	± 1 %	± 1 %	-	± 0.1
F_XC72R	Film casting	XC-72R	3.5	23.4	-	-	73.1	1	17.1
S_XC72R	Spray	XC-72R	0.1	0.7	-	-	99.2	160	18.5
F_X85_0.5µm	Film casting	X85	3.5	23.4	-	-	73.1	1	19.8
S_X85_0.5µm_A	Spray	X85	0.1	0.7 [a]	-	-	99.2	160	20.3
S_ X85_0.5µm _B	Spray	X85	0.1	0.7 [a]	-	-	99.2	320	42.2
S_X85_7µm	Spray	X85	0.22	-	1.09	55.5	43.2	69	24.4

Table 2: Thickness, roughness and density measured by profilometry or 3D laser scanning microscopy.

	Profilometry			3D laser scanning microscopy	
	Mean thickness	**Roughness**	**Density**	**Mean thickness**	**Roughness**
	(µm)	(µm)	(g cm^{-3})	(µm)	(µm)
	± 0.1	± 0.1	± 0.1	± 0.1	± 0.1
F_XC72R	4.8	0.2	1.4	(6.4)[b]	0.1
S_XC72R	6.3	0.6	1.2	5.7	0.8
F_X85_0.5µm	7.8	0.3	1.0	(7.1)[b]	0.3
S_X85_0.5µm_A	8.5	1.4	1.0	-[a]	-[a]
S_X85_0.5µm_B	16.4	2.8	1.0	-[a]	-[a]
S_X85_7 µm	12.9	2.8	0.8	10.1	3.0

[a] Not measured; [b] values not representative of the whole sample because as shown in sections 3.1 and 3.2, the thickness is not homogeneous over the whole sample.

Table 3: Comparison of the mean thickness obtained by simulating the motion of the profilometer tip on the 3D microscopy profile with the experimental 3D microscopy and profilometry measurements.

	$D_{micro\ 3D}$ [a] (%)	$D_{profilometry}$ [b] (%)
	± 1	± 1
F_XC72R	3	- [c]
F_X85_0.5µm	6	- [c]
S_XC72R	10	1
S_X85_7 µm	45	-10

[a] $D_{micro\ 3D}$ is the difference between the thickness obtained by the simulation of the tip and the 3D laser microscopy thickness calculated by : $\frac{\text{Thickness}_{\text{simulation}} - \text{Thickness}_{\text{micro 3D}}}{\text{Thickness}_{\text{micro 3D}}}$

[b] $D_{profilometry}$ is the difference between the thickness obtained by the simulation of the tip and the profilometry thickness calculated by : $\frac{\text{Thickness}_{\text{simulation}} - \text{Thickness}_{\text{profilometry}}}{\text{Thickness}_{\text{profilometry}}}$

[c] Values not representative of the whole sample.

Declaration of interests

☒ The authors declare that they have no known competing financial interests or personal relationships that could have appeared to influence the work reported in this paper.

☐The authors declare the following financial interests/personal relationships which may be considered as potential competing interests: